Cell Reports

Article

Focal clusters of peri-synaptic matrix contribute to activity-dependent plasticity and memory in mice

Graphical abstract

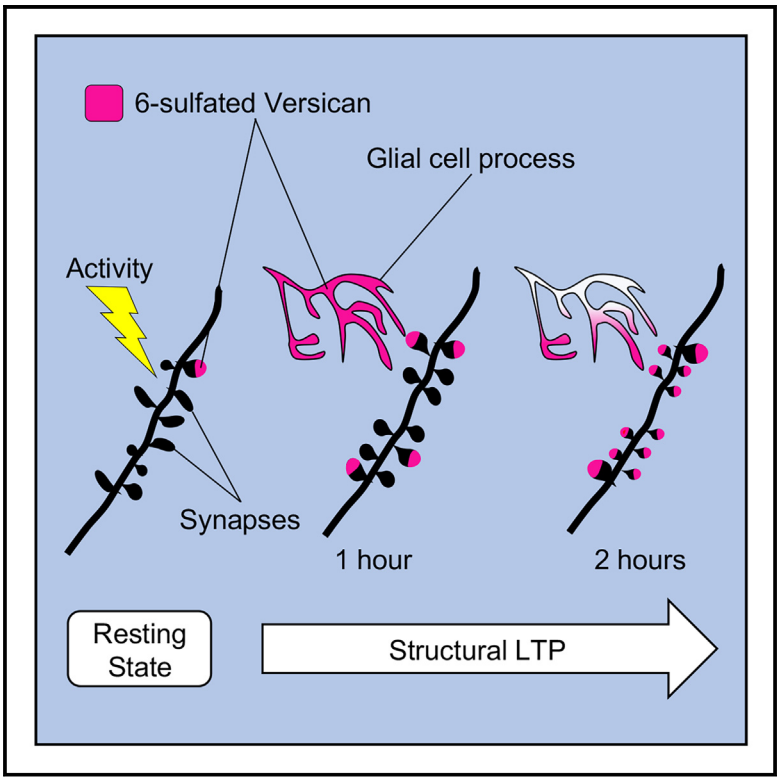

Authors

Gabriele Chelini, Hadi Mirzapourdelavar, Peter Durning, ..., Yuri Bozzi, Alexander Dityatev, Sabina Berretta

Correspondence

s.berretta@mclean.harvard.edu

In brief

Chelini et al. demonstrate that versican regulates the expression of a specific proteoglycan glycoform, contributing to long-term potentiation and hippocampal-dependent memory in mice. These findings bring attention to a potential mechanism contributing to the spatial arrangement of synaptic ensembles during the active phase of experience-dependent plasticity.

Highlights

- Glia-derived chondroitin sulfate (CS) proteoglycans form aggregates of peri-synaptic matrix
- Clusters of peri-synaptic matrix arise in an experience-dependent fashion
- Versican core protein regulates the expression of a specific 6-sulfated CS glycoform
- 6-sulfated CS contributes to spatially organized synaptic refinement

Chelini et al., 2024, Cell Reports *43*, 114112
May 28, 2024
https://doi.org/10.1016/j.celrep.2024.114112

CellPress

Cell Reports

CellPress
OPEN ACCESS

Article

Focal clusters of peri-synaptic matrix contribute to activity-dependent plasticity and memory in mice

Gabriele Chelini,[1,2,3,15] Hadi Mirzapourdelavar,[4,15] Peter Durning,[1] David Baidoe-Ansah,[4] Manveen K. Sethi,[5] Sinead M. O'Donovan,[6] Torsten Klengel,[2,7,8] Luigi Balasco,[3] Cristina Berciu,[1] Anne Boyer-Boiteau,[1] Robert McCullumsmith,[6] Kerry J. Ressler,[2,9,10] Joseph Zaia,[5,11] Yuri Bozzi,[3,12,16] Alexander Dityatev,[4,13,14,16] and Sabina Berretta[1,2,9,16,17,*]

[1]Translational Neuroscience Laboratory, McLean Hospital, Belmont, MA 02478, USA
[2]Department of Psychiatry, Harvard Medical School, Boston, MA 02215, USA
[3]Center for Mind/Brain Sciences, University of Trento, Rovereto 38068 Trento, Italy
[4]Molecular Neuroplasticity Group, German Center for Neurodegenerative Diseases, Magdeburg 39120 Saxony-Anhalt, Germany
[5]Center for Biomedical Mass Spectrometry, Department of Biochemistry and Cell Biology, Boston University School of Medicine, Boston, MA 02118, USA
[6]Cognitive Disorders Research Laboratory, University of Toledo, Toledo, OH 43606, USA
[7]Translational Molecular Genomics Laboratory, Mclean Hospital, Belmont, MA 02478, USA
[8]Department of Psychiatry, University Medical Center Göttingen, 37075 Göttingen, Germany
[9]Program in Neuroscience, Harvard Medical School, Boston, MA 02215, USA
[10]Neurobiology of Fear Laboratory, McLean Hospital, Belmont, MA 02478, USA
[11]Bioinformatics Program, Boston University, Boston, MA 02215, USA
[12]CNR Neuroscience Institute Pisa, 56124 Pisa, Italy
[13]Medical Faculty, Otto von Guericke University, Magdeburg 39106 Saxony-Anhalt, Germany
[14]Center for Behavioral Brain Sciences, Otto von Guericke University, Magdeburg 39106 Saxony-Anhalt, Germany
[15]These authors contributed equally
[16]Senior author
[17]Lead contact
*Correspondence: s.berretta@mclean.harvard.edu
https://doi.org/10.1016/j.celrep.2024.114112

SUMMARY

Recent findings show that effective integration of novel information in the brain requires coordinated processes of homo- and heterosynaptic plasticity. In this work, we hypothesize that activity-dependent remodeling of the peri-synaptic extracellular matrix (ECM) contributes to these processes. We show that clusters of the peri-synaptic ECM, recognized by CS56 antibody, emerge in response to sensory stimuli, showing temporal and spatial coincidence with dendritic spine plasticity. Using CS56 co-immunoprecipitation of synaptosomal proteins, we identify several molecules involved in Ca^{2+} signaling, vesicle cycling, and AMPA-receptor exocytosis, thus suggesting a role in long-term potentiation (LTP). Finally, we show that, in the CA1 hippocampal region, the attenuation of CS56 glycoepitopes, through the depletion of versican as one of its main carriers, impairs LTP and object location memory in mice. These findings show that activity-dependent remodeling of the peri-synaptic ECM regulates the induction and consolidation of LTP, contributing to hippocampal-dependent memory.

INTRODUCTION

A critical challenge in neurobiology is to understand how neuronal activity refines local brain circuitry, resulting in experience-dependent learning. Converging evidence suggests that coordinated remodeling of adjacent synapses represents an efficient mechanism for the acquisition and storage of novel information.[1–6] These studies show that the strength of a group of neighboring synapses on a dendritic segment increases within 90 min of a sensory stimulus.[4,6,7] Thereafter, approximately 2 h following the triggering stimulus, the majority of newly potentiated synapses is reached by the protein product of the immediate-early gene (IEG) Arc/Arg3.1 (ARC), which drives massive activity-dependent heterosynaptic long-term depression (hLTD).[4,5,7] As a consequence, only a small fraction of newly potentiated synapses are stabilized and functionally integrated into the local circuitry.[4–6] This harmonized biphasic process results in an organized spatial arrangement of synaptic ensembles (i.e., synaptic clustering), putatively optimizing the signal-to-noise ratio within the local microcircuitry and providing a suitable substrate for

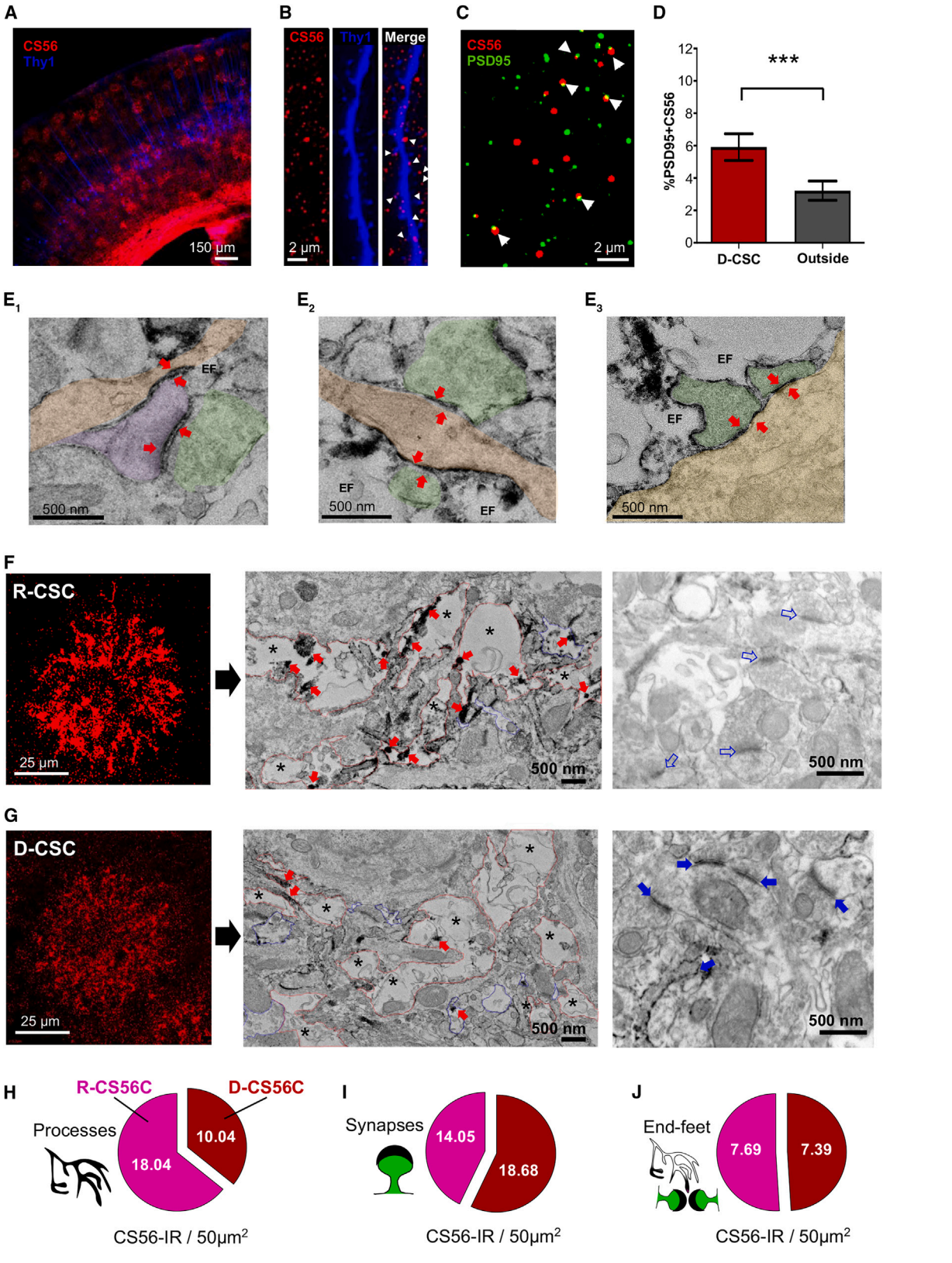

(legend on next page)

the implementation of newly acquired information into the biological system.[1–6]

We reasoned that a coordinated remodeling of neighboring synapses requires massive restructuring of the local extracellular space, thus involving distinguishable changes in the peri-synaptic extracellular matrix (ECM). Indeed, converging findings show that specific ECM molecules, chondroitin sulfate proteoglycans (CSPGs), are key functional components of synaptic extracellular scaffolding, embedding pre- and post-synaptic terminals and powerfully regulating the actin cytoskeleton, synaptic plasticity,[8–17] and memory consolidation.[18,19] Accordingly,[20] enzymatic digestion of CSPGs enhances the motility of dendritic spines,[14] reinstates a juvenile-like form of experience-dependent plasticity,[17] and promotes the erasure of fear memories.[19] Importantly, previous studies showed that CSPGs' role in synaptic plasticity largely depends on the chemical composition of glycosaminoglycan (GAG) chains, which can be alternatively sulfated in position 2, 4, or 6 of the N-acetyl-galactosamine sugar chains.[10] Specifically, sulfation in position 6 was shown to positively mediate synaptogenesis, enhancing the establishment of synaptic contacts.[11,21–23] This makes it an ideally suitable molecular player to participate in the dynamic and acute phase of local synaptic remodeling.

In primates and rodents, immunolabeling using CS56 antibodies recognizing 6- and 2,6-sulfated chondroitin sulfates[24] results in morphologically conserved round structures populating cortical and subcortical brain regions,[10,25–27] namely CS clusters (CSCs). While CSCs have been previously described in both human and rodent postmortem brain,[25–27] their biological function remains unknown. Here, we show that, across species and brain areas, these structures present in distinct morphological conformations, from a cluster of sharply labeled converging processes (rosette CSCs; R-CSCs) to a group of diffuse puncta (diffuse CSCs, D-CSCs). We also show that the prevalence of R-CSCs and D-CSCs in the mouse barrel cortex (BCx) dynamically changes in response to naturalistic whisker stimulation, following a temporal profile consistent with the timing of synaptic structural plasticity. Consistently, we report that CSCs' alternative conformations relate to specific geometrical features of dendritic spines and are paralleled by the dendritic expression of ARC. Finally, we discovered that the CS56 sulfation pattern is largely associated with the CSPG core protein versican (Vcan), and downregulation of Vcan selectively impairs the expression of chondroitin-6-O-sulfotransferase 2 (Chst7) *in vitro* and *in vivo*. Accordingly, hippocampal downregulation of Vcan-CS56 impairs long-term potentiation (LTP) and object location memory in adult mice, indicating that 6-sulfated CSPG Vcan plays a key role in learning, memory, and synaptic plasticity.

RESULTS

CSCs show ultrastructural association with synapses and glial cells

We initially confirmed that immunolabeling using CS56 antibody on brain tissue resulted in widespread labeling of CSCs, which appeared along a spectrum of morphological configurations. For the purpose of this study, CSCs were classified into two main types, R-CSCs and D-CSCs, which correspond to the extremes of the whole morphological spectrum (Figure S1); this suggests that D-CSCs and R-CSCs may represent different transient stages of the same structure. Details for CSC morphological classification are reported in the STAR Methods (under "details for elements quantification in microscopy experiments," subsection "CSCs classification"). Both D-CSCs and R-CSCs were detected in cortical and subcortical brain regions, across multiple mammalian species (human, non-human primates, and rodents; Figure S2). To investigate CS56 location in the synaptic scaffolding, we started by performing immunostaining with the CS56 antibody in the BCx, an area that is commonly densely populated by CSCs, in Thy1-eYFP mice,[28] assessing their relationship with apical dendrites of layer 2/3. We found that CSCs encompass multiple dendrites (Figure 1A) and that CS56-immunoreactive (CS56-IR) puncta are recurrently juxtaposed to Thy-1-labeled dendritic spines (Figure 1B). To further establish the broad-scale association between CS56 immunoreactivity and excitatory synapses, we quantified PSD95-IR post-synaptic elements juxtaposed to CS56-IR puncta within and outside of CSCs (Figure 1C). Within CSCs, 6% of PSD95-IR elements were contiguous to CS56-IR puncta. This percentage was significantly lower (3%) in equivalent, adjacent areas outside the CSCs (Figure 1D; Table S1). These findings indicate that CS56-reactive CSPGs form aggregates of peri-synaptic ECM and that this association occurs predominantly within CSCs.

Figure 1. CS56 forms peri-synaptic coating within and outside of CSCs

(A) Thy-1-positive apical dendrites intersect several CSCs within multiple layers of the mouse barrel cortex. Scale bar, 150 μm.

(B) CS56 punctate labeling is juxtaposed to Thy-1-positive dendritic spines (arrowheads). Scale bar, 2 μm.

(C) Representative photomicrograph showing sparse juxtaposition (arrowheads) of PSD95-IR and CS56-IR puncta outside CSCs. Scale bar, 2 μm.

(D) The percentage of PSD95-IR puncta juxtaposed to CS56-IR puncta is higher within D-CSCs with respect to adjacent areas. n = 5 D-CSCs and 5 control images from three mice. D-CSC mean = 5.82, SEM = 0.59, t test; control mean = 3.22, SEM = 0.59; p = 0.0004, 95% confidence interval (CI) −4.025 to −1.357.

(E) Examples of CS56 immunoreactivity (red arrow) associated with synapses: (E_1) dendritic spine (in purple), (E_2) axodendritic synapses, and (E_3) axosomatic synapses. Pre-synaptic elements are highlighted in green. Post-synaptic elements are highlighted in yellow. Scale bar, 500 nm.

(F and G) CS56 ultrastructural location within R-CSCs and D-CSCs. Left: representative confocal photomicrograph of one R-CSC (F) and one D-CSC (G) (asterisks mark glial processes; scale bar, 25 μm). Center: CS-IR products within glial cell processes (red arrows) for both R-CSC (F) and D-CSC (G). Scale bar, 500 nm. Right: the difference between CS56-immunonegative (empty blue arrows) and immunopositive (blue-filled arrows) synapses within R-CSCs (F) and D-CSCs (G). Scale bar, 500 nm. Glial processes are circumscribed in red, endfeet in blue.

(H–J) Pie charts depicting the absolute number of CS56-IR elements within one prototypical R-CSC and one D-CSC. (H) R-CSCs present with predominant CS56 immunoreactivity within glial processes. (I) In contrast, D-CSCs present with higher numbers of CS56-IR synaptic coatings. (J) Similar amounts of CS56 immunoreactivity in glial endfeet are observed in R-CSCs and D-CSCs.

Error bars indicate SEM. ***$p < 0.0001$.

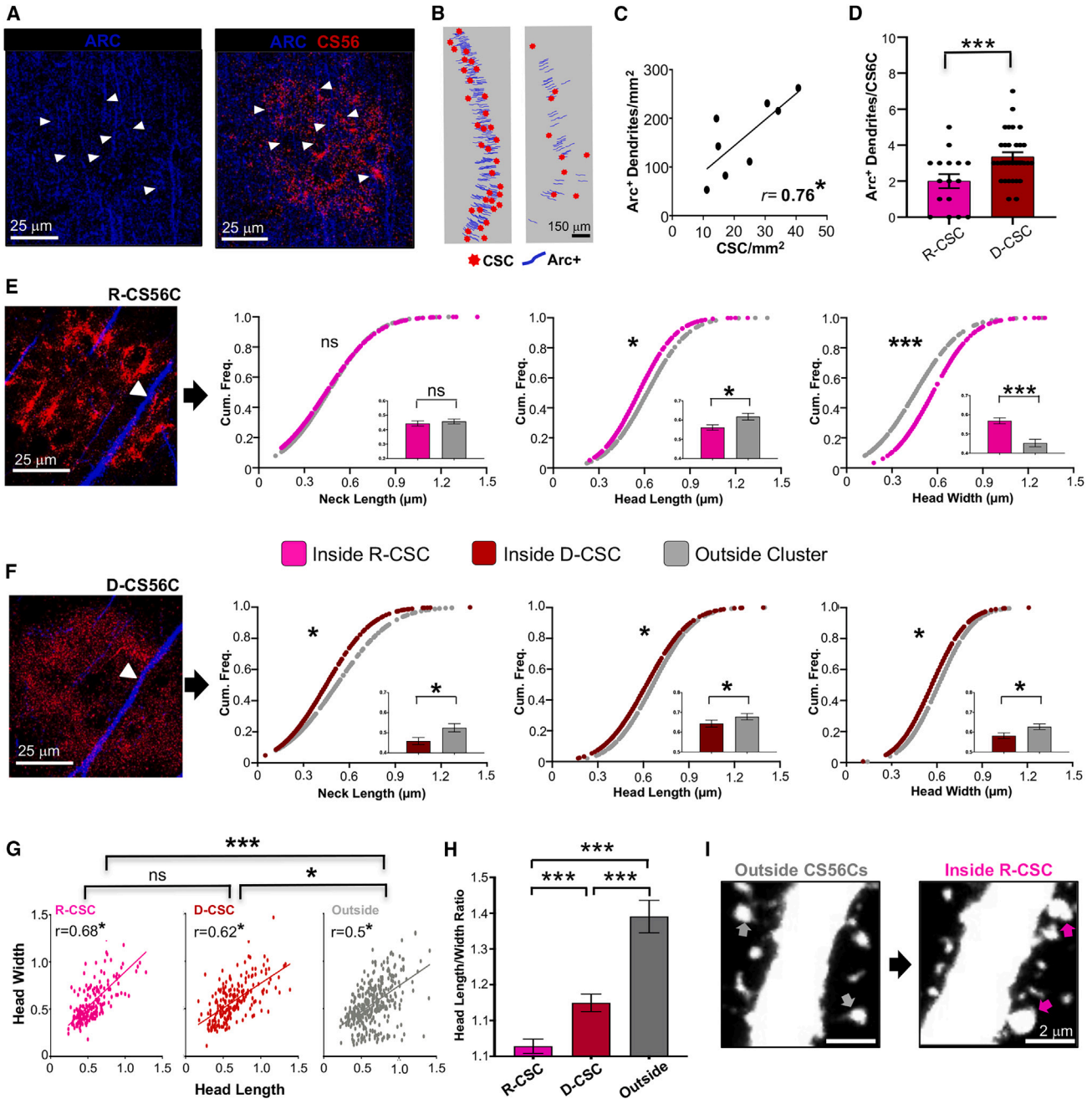

Figure 2. In the barrel cortex of naive home-caged mice, CSCs present molecular and subcellular features associated with activity-dependent plasticity

(A) Confocal photomicrographs showing multiple ARC-IR dendrites (white arrowhead) within D-CSCs in the mouse BCx. Scale bar, 25 μm.

(B) Virtual maps depicting the distribution of CSCs (red stars) and ARC-positive dendrites (blue lines) in two representative subjects. The left image shows the concomitant high density of both CSCs and ARC$^+$ dendrites; the right image shows low density of both elements. Scale bar, 150 μm.

(C) The number of CSCs positively correlates with ARC-IR dendrites within the BCx. n = 8 slices from four mice. r = 0.76, p = 0.02, CI 0.1312 to 0.9549.

(D) D-CSCs contain higher numbers of ARC$^+$ dendrites compared to R-CSCs. R-CSCs n = 17, mean = 1.88, SEM = 0.37; D-CSCs n = 31, mean = 3.35, SEM = 0.24; from four animals; t test p = 0.003; CI 0.4631 to 2.247.

(E) Within R-CSCs, dendritic spines present wider and shorter heads, but unaltered necks compared to outside CSCs. n = 194 spines within R-CSCs, n = 154 control spines over four dendrites from four different animals. Mann-Whitney: neck length, R-CSCs mean = 0.44, SEM = 0.01; control mean = 0.45, SEM = 0.01; p = 0.347, CI −0.02 to 0.06. Head length, R-CSCs mean = 0.56, SEM = 0.01; control mean = 0.61, SEM = 0.01; p = 0.004, CI 0.02 to 0.1. Head width, R-CSCs mean = 0.56, SEM = 0.01; control mean = 0.45, SEM = 0.01; p < 0.0001, CI −0.17 to −0.07. The photomicrograph on the left shows an example of an R-CSC containing layer 2/3 apical dendrites. Scale bar, 25 μm.

(legend continued on next page)

To confirm CS56 immunoreactivity's ultrastructural location in the peri-synaptic space, we imaged two prototypical CSCs (one R-CSC and one D-CSC) using transmission electron microscopy after pre-embedding CS56 immunolabeling. We found that CS56-IR product coats a highly heterogeneous synaptic population. CS56 immunoreactivity was observed around dendritic spines, filling the synaptic cleft (Figures 1E$_1$, S3, and S4), as well as axodendritic and axosomatic boutons (Figures 1E$_2$, E$_3$, and S3), thus implying an association with both excitatory and inhibitory contacts.[29,30] This mixed distribution suggests that CS56 might be a pleiotropic factor whose role in the synaptic machinery is shared across diverse neuronal populations.

Moreover, within CSCs, CS56 immunoreactivity was also enriched within glial endfeet and glial processes, predominantly overlapping with the intermediate filaments (Figures 1F, 1G, and S3). No CS56 immunoreactivity was detected within neuronal cell bodies or dendrites (Figure S3). Notably, key similarities and differences were detected between D-CSCs and R-CSCs (Figures 1F–1J). For R-CSCs, CS56 immunoreactivity was predominantly observed within glial cells, in larger proportions compared to D-CSCs (Figures 1F, 1G, and 1H). Conversely, a higher proportion of synapses coated with CS56 peri-synaptic labeling was found in D-CSCs with respect to R-CSCs (Figures 1F, 1G, and 1I). Similar proportions of CS56-IR glial endfeet were found in both CSC types (Figures 1F, 1G, and 1J).

These results illuminate the CSC structure, composed of glial processes and endfeet and extracellular peri-synaptic coatings of 6-sulfated chondroitin sulfate moiety. Furthermore, the differential distribution of CS56 immunoreactivity accounts for the distinct morphology of CSCs, i.e., R-CSCs showing a predominance of large glial processes and D-CSCs presenting prevalent synaptic coatings, resulting in a punctate appearance (Figure S1). Finally, the lack of CS56 immunoreactivity within neuronal cell bodies corroborates previous transcriptomic data showing predominant expression of Chst7 within astrocytes and polydendrocytes[31] (http://dropviz.org/) and suggests that glial cells actively provide CS56 coating onto neighboring synapses.

CSCs show spatial association with ARC/Arg3.1 dendritic expression

Convergent accumulation of CS56 within glial cell processes and nearby synaptic terminals led us to hypothesize that CSCs might be reflective of an active process of local synaptic remodeling where glial cells provide peri-synaptic CSPG coating to a synaptic ensemble in an activity-dependent fashion. We reasoned that, if this is the case, CSCs unpredictable distribution within the BCx may be accompanied by similar expression of IEGs within the same region.

To test this hypothesis, we quantified both the number of CSCs and the number of dendrites immunopositive for the protein product of the IEG ARC/Arg3.1 (ARC$^+$ dendrites) in the BCx layer 2/3, using multiple fluorescent immunolabeling in a group of naive home-caged mice (Figure 2A). ARC was chosen as an ideal indicator for activity-dependent plasticity, as it is known to travel along dendritic branches to reach specific synaptic target locations. Once at synapses (approximately 2 h following a triggering stimulus), ARC promotes the spatial arrangements of neighboring terminals (i.e., synaptic clustering) in an activity-dependent manner.[4] We found that an increased number of ARC$^+$ dendrites in the BCx was accompanied by an increased number of CSCs in the same region, as testified by a strong positive correlation between the two elements (Figures 2B and 2C). This observation is consistent with the idea that CSCs and ARC might be similar indicators of activity-dependent plasticity. Then, we found that the number of ARC$^+$ dendrites contained within D-CSCs was significantly higher in comparison to R-CSCs (Figure 2D). The preferential association between ARC$^+$ dendrites and D-CSCs suggests that this morphology might present in temporal coherence with the ARC role in synaptic clustering, occurring 2 h following a triggering stimulus.[4] Taken together, these data support the idea that CSCs highlight focal sites of locally coordinated plasticity and suggest that R-CSCs' and D-CSCs' morphological transition might occur in a time frame consistent with the plateauing phase of structural LTP (s-LTP, 1–2 h after a stimulus) and prior to the occurrence of hLTD (after 2 h).[4,7]

Dendritic spines contained within CSCs present morphometric features consistent with localized shifts in synaptic strength

The association of CS56 immunoreactivity with synapses is consistent with a well-established role of CSPGs in regulating synaptic plasticity.[8–12,16–19,21,22] Furthermore, denser presence of CS56-immunopositive glial processes within R-CSCs suggests that non-cell-autonomous CS56 accumulation around synapses might occur at an earlier stage of local synaptic remodeling, characterized by widespread s-LTP. Conversely, spatial

(F) Within D-CSCs, dendritic spines are smaller compared to spines located outside CSCs. n = 216 spines within D-CSCs, n = 206 control spines over six dendrites from four different animals. Mann-Whitney: neck length, D-CSCs mean = 0.44, SEM = 0.01; control mean = 0.51, SEM = 0.01; p = 0.012, CI 0.01 to 0.1. Head length, D-CSCs mean = 0.63, SEM = 0.01; control mean = 0.66, SEM = 0.01; p = 0.047, CI 0 to 0.09. Head width, D-CSCs mean = 0.57, SEM = 0.01; control mean = 0.61, SEM = 0.01; p = 0.024, CI 0 to 0.08. The photomicrograph on the left shows an example of a D-CSC containing layer 2/3 apical dendrites. Scale bar, 25 μm. White arrowheads identify the dendrites that were used for dendritic spine analysis for the given images.

(G) The correlation between spine head length and width is stronger within CSCs. Length-width correlation: R-CSCs r = 0.689, $p < 0.0001$, CI 0.6075 to 0.7567; D-CSCs r = 0.621, $p < 0.0001$, CI 0.5325 to 0.6974; control r = 0.509, $p < 0.0001$, CI 0.4288 to 0.5827. Z test: R-CSCs vs. D-CSCs p = 0.23; R-CSCs vs. control p = 0.001; D-CSCs vs. control p = 0.04.

(H) Spines within R-CSCs are stubbier than outside CSCs, while spines within D-CSCs present with intermediate geometrical relationships: length/width ratio, R-CSCs mean = 1.029, SEM = 0.01; D-CSCs mean = 1.149, SEM = 0.02; controls mean = 1.39, SEM = 0.04. t test: R-CSCs vs. D-CSCs $p < 0.0001$, CI 0.05757 to 0.1837. R-CSCs vs. control $p < 0.0001$, CI 0.2371 to 0.4868. D-CSCs vs. control $p < 0.0001$, CI 0.1205 to 0.3621.

(I) Confocal photomicrographs showing spines with large heads and short necks within R-CSCs (magenta arrows)—outside CSC spines have narrower heads and longer necks (gray arrows). Scale bar, 2 μm.

Error bars indicate SEM. $^*p < 0.05$, $^{**}p < 0.001$, $^{***}p < 0.0001$.

overlap between ARC$^+$ dendrites and D-CSCs might coincide with a later stage. To test this hypothesis, we used dendritic spine morphology as a structural proxy for synaptic strength,[4,32–34] comparing the population of spines embedded within vs. control spines located outside CSCs (both R-CSCs and D-CSCs), in a group of naive Thy1-eYFP mice (BCx, layer 2/3). Our results showed that mushroom spines within R-CSCs have significantly wider heads and decreased head length with respect to control spines, with a length-to-width ratio of ~1 (Figure 2E). Conversely, spines within D-CSCs showed a significant decrease in head width and length as well as neck length (Figure 2F). In all three conditions we found that spine head length and width strongly correlated with each other (Figure 2G), but the strength of this correlation was significantly higher within CSCs (Figure 2G), demonstrating that the synaptic population included in CSCs displays remarkable morphological homogeneity. Consequentially, the spine head length-to-width ratio was significantly different between the three experimental conditions (Figure 2H), with R-CSCs showing stubbier heads (ratio = 1.028) compared to the thinner control spines (ratio = 1.39) and to the intermediate morphology observed in D-CSCs (ratio = 1.149). No significant differences were found between dendritic spine densities within and outside of CSCs (Figure S5; Table S2). These results show that dendritic spines are significantly larger, and putatively potentiated, within R-CSCs, while spines contained within D-CSCs present an intermediate morphology between R-CSCs and controls (Figures 2H and 2I; Table S3). These findings corroborate our hypothesis suggesting that R-CSCs emerge during an earlier phase, temporally matching the peak of local synaptic strength resulting from widespread s-LTP. Conversely, D-CSC morphology occurs at a later stage, consistent with the role of ARC in synaptic clustering.

Sensory experience affects the number of CSCs in rodent BCx

Our findings indicate that R-CSCs and D-CSCs may represent sequential stages of the same transient process of activity-dependent rearrangement of peri-synaptic ECM. Specifically, R-CSCs might be associated with an earlier phase of s-LTP, while D-CSCs might correspond to the endpoint of this process and the beginning of targeted hLTD. However, for this to be true, R-CSCs and D-CSCs need to emerge in an activity-dependent manner and match the temporal progression of clustered plasticity occurring within 2 h of a triggering stimulus.[3,4] To test this hypothesis, we assessed whether sensory manipulations had an impact on the number of CSCs within the mouse BCx. To do so, we started by comparing the number of CSCs between hemispheres 1 week following unilateral whisker trimming (Figure 3A). First, we noted that, under standard conditions, R-CSCs are slightly more numerous in layer 2/3 compared to D-CSCs, while the density of both R-CSCs and D-CSCs is consistent across cortical layers (Figure S6A). This observation may simply be a consequence of the R-CSC and D-CSC half-life, which renders R-CSCs well distinguishable for longer periods of time. More importantly, we established that there is no difference between left and right hemispheres (Figures 3B, 3C, S6B, and S6C). Conversely, in a group of whisker-deprived mice, the numerical densities (NDs) of CSCs were reduced in the BCx contralateral to whisker trimming compared to the ipsilateral side (Figures 3B, 3C, S6B, and S6C; Table S4). This difference was mostly driven by significant changes detectable in layer 2/3 and layer 5 (Figure 3D) and affected both R-CSCs and D-CSCs alike (Figure 3E). Then, to test whether sensory stimulation was able to induce CSC formation in the BCx, we delivered a passive multi-whisker stimulation in anesthetized mice using a wooden stick,[35] known to induce layer-5-specific synaptic activation[36,37] (Figure 3F). Animals were sacrificed at 1 and 2 h after the stimulation session. At 1 h, R-CSCs, but not D-CSCs, were significantly increased in layer 5 selectively (Figures 3G and S6D; Table S5). Conversely, D-CSCs, but not R-CSCs, were significantly increased after 2 h in the same layer (Figures 3H and S6E; Table S5). No significant changes in either category were observed when the post-stimulus interval was extended to 4 h (Figure S6F). Moreover, no interhemispheric difference was found in motor cortex layer 5, a brain region putatively unaffected by the stimulation, excluding the possibility of stimulus-independent interhemispheric biases (Figure S6G). Together, these findings confirm that neuronal activity is both necessary and sufficient to induce CSC formation, putatively accounting for their sparse and unpredictable anatomical distribution and corroborating our previous findings. Altogether our findings establish that CSCs present molecular (ARC), subcellular (spine geometry), and temporal features consistent with an ongoing process of activity-dependent remodeling of locally coordinated synapses.

CS56 immunoprecipitation from crude synaptosomal fractions suggests a pivotal role in LTP

CSPGs are ascribed diverse biological functions based on their molecular composition.[10,13] To gain further insights into the synaptic role of CS5-reactive CSPGs, we used the CS56 antibody to immunoprecipitate 6-sulfated chondroitin sulfate-carrying core proteins and their interaction partners. Before immunoprecipitation (IP), freshly dissected extracts of mouse primary somatosensory cortex were fractionated to obtain two separate preparations (Figure 4A).[38] The supernatant (S2), resulting from the fractionation and containing the light-membrane compartments (Figure 4A), was used to investigate the extracellular binding partners and core proteins. The pellet (P2), enriched in crude synaptosomal fractions (Figure 4A), was collected to identify proteins interacting with CS56-reactive glycans within the synaptic machinery. Prior to the IP, protein lysates obtained from both S2 and P2 fractions were tested for the presence of CS56-reactive CSPGs using western blotting. We confirmed the presence of a CS56-specific band localized at approximately 80 kDa molecular weight in both preparations (Figure 4B). After IP, the CS56-specific band was isolated on a gel run using Coomassie blue staining and excised for liquid chromatography-tandem mass spectrometry (LC-MS/MS) proteomics. Figure 4C shows the location of the band used for proteomics identified using silver staining. In the light microsomal (LM) fractions, we identified all four CSPG core proteins of the lectican family after CS56 IP. Among them, Vcan and brevican were significantly more abundant than both aggrecan and neurocan (Figure 4D; Table S6). CS56 IP confirmed the presence of Vcan, brevican, and neurocan in the postmortem human amygdala (Figures 4E

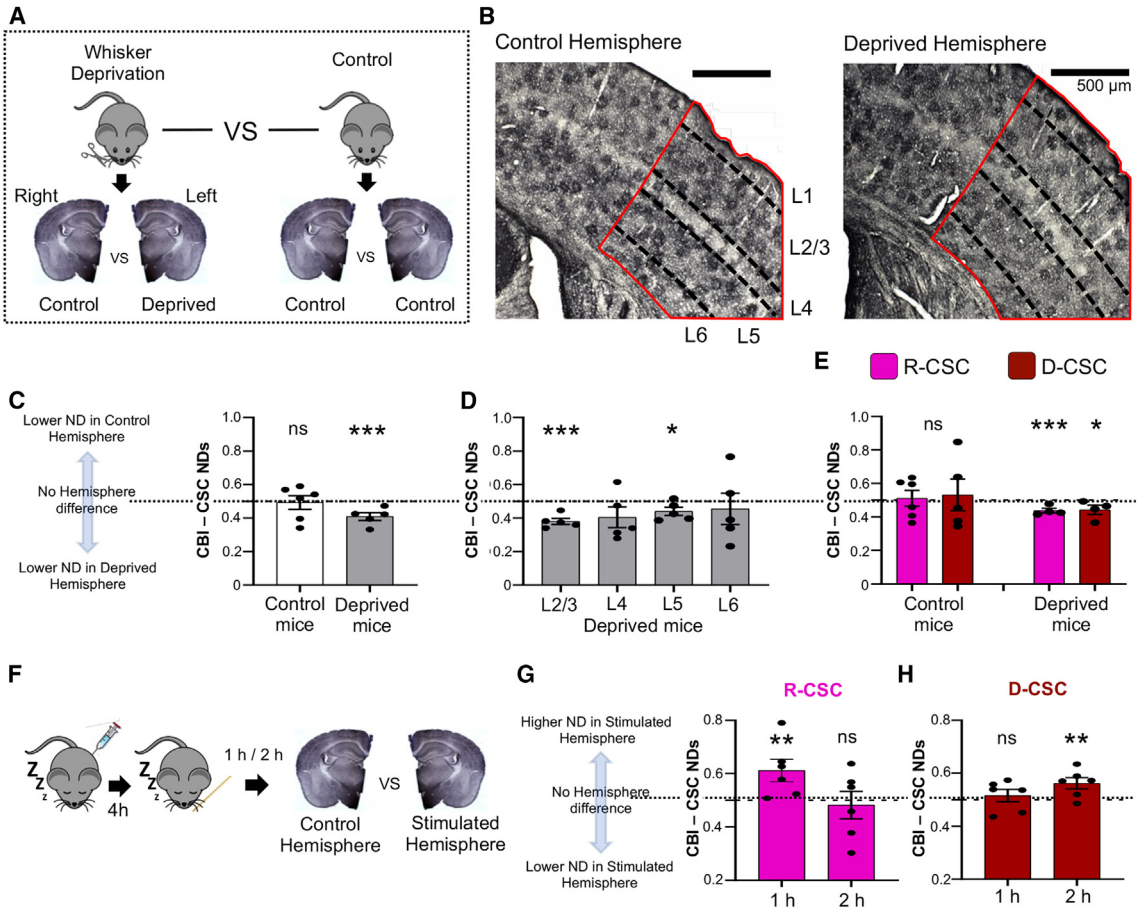

Figure 3. Sensory experience affects numerical densities of CSCs in the BCx

(A) Experimental design for sensory deprivation experiment.

(B) Representative photomicrographs depicting reduced CSC numerical densities (NDs) in the BCx of a sensory-deprived hemisphere (right) compared to a non-deprived hemisphere (left). Red contouring highlights the BCx. Scale bar, 500 µm.

(C) Sensory deprivation shifts CSC NDs in favor of the non-deprived hemisphere in deprived mice, while controls show a comparable number of CSCs across hemispheres. Deprived $n = 5$; controls $n = 6$; Z test contralateral bias index (CBI): controls mean = 0.49, SEM = 0.04; $p = 0.86$, CI −0.1130 to 0.09871. Deprived mean = 0.4, SEM = 0.02; $p = 0.0001$, CI −0.1545 to −0.02621.

(D) This result is mostly driven by significant changes affecting predominantly layers 2/3 and 5. Z test CBI layer 2/3: deprived mean = 0.39, SEM = 0.01; $p < 0.0001$, CI −0.1692 to −0.06925. CBI layer 5: deprived mean = 0.45, SEM = 0.02; $p = 0.013$, CI −0.1273 to 0.007380.

(E) Both R-CSCs and D-CSCs decrease following whisker deprivation. Z test CBI R-CSCs: controls mean = 0.51, SEM = 0.0471; $p = 0.81$, CI −0.1102 to 0.1323, $n = 5$; deprived mean = 0.43, SEM = 0.0471; $p < 0.0001$, CI −0.1067 to −0.01829, $n = 5$. Z test CBI D-CSCs: controls mean = 0.53, SEM = 0.0938; $p = 0.72$, CI -0.2292 to 0.2922, $n = 5$; deprived mean = 0.44, SEM = 0.0272; $p = 0.03$, CI −0.1438 to 0.02960, $n = 4$.

(F) Experimental design for sensory stimulation.

(G and H) R-CSCs increase 1 h post-stimulation in layer 5 of the BCx. $n = 6$ stimulated, $n = 6$ controls. Z test CBI R-CSCs mean = 0.61, SEM = 0.03; $p = 0.017$, CI 0.003703 to 0.2200. D-CSCs mean = 0.48, SEM = 0.02; $p = 0.496$, CI −0.04495 to 0.07607. Conversely, D-CSCs selectively increase at 2 h post-stimulation. $n = 6$ stimulated, $n = 6$ controls. Z test CBI: R-CSCs mean = 0.48, SEM = 0.05; $p = 0.727$, CI −0.1503 to 0.1148; D-CSCs mean = 0.58, SEM = 0.01; $p < 0.003$, CI 0.006922 to 0.1168. Error bars indicate SEM. $^{*}p < 0.05$, $^{**}p < 0.001$, $^{***}p < 0.0001$.

and S7; Table S7), a brain region previously shown to be affected by a significant reduction in CSCs in people with psychiatric illnesses.[26]

Then, KEGG pathway analysis on CS56 immunoprecipitate P2 revealed the presence of several proteins involved in synaptic vesicle recycling that belong to the SNARE complex[39] (17 genes, $p = 2.3e{-}12$). Among these, we identified synaptotagmins (SYT 1, 2, and 7), synapsins (SYN 1–3), synaptogyrins (SYG 1–3), synaptic vesicle glycoproteins 2 (SV2A and B) and synaptophysin (SYPH) (Figure 4E; Table S8). All these proteins play a well-established role in active plasticity sites promoting vesicle docking, Ca^{2+}-dependent exocytosis of the α-amino-3-hydroxy-5-methyl-4-isoxazolepropionic acid (AMPA) receptor, and induction of LTP.[40–45] Consistently, LTP was also identified by pathway analysis (six genes, $p = 1.2e{-}2$). Finally, we found that CS56 synaptic carriers/binding partners belong to a heterogeneous synaptic population (i.e., glutamatergic [seven genes, $p = 2.9e{-}2$], GABAergic [seven genes, $p = 9.7e{-}3$], dopaminergic [nine genes, $p = 6.5e{-}3$], and cholinergic [six genes, $p = 8e{-}2$]), confirming our electron microscopy (EM)

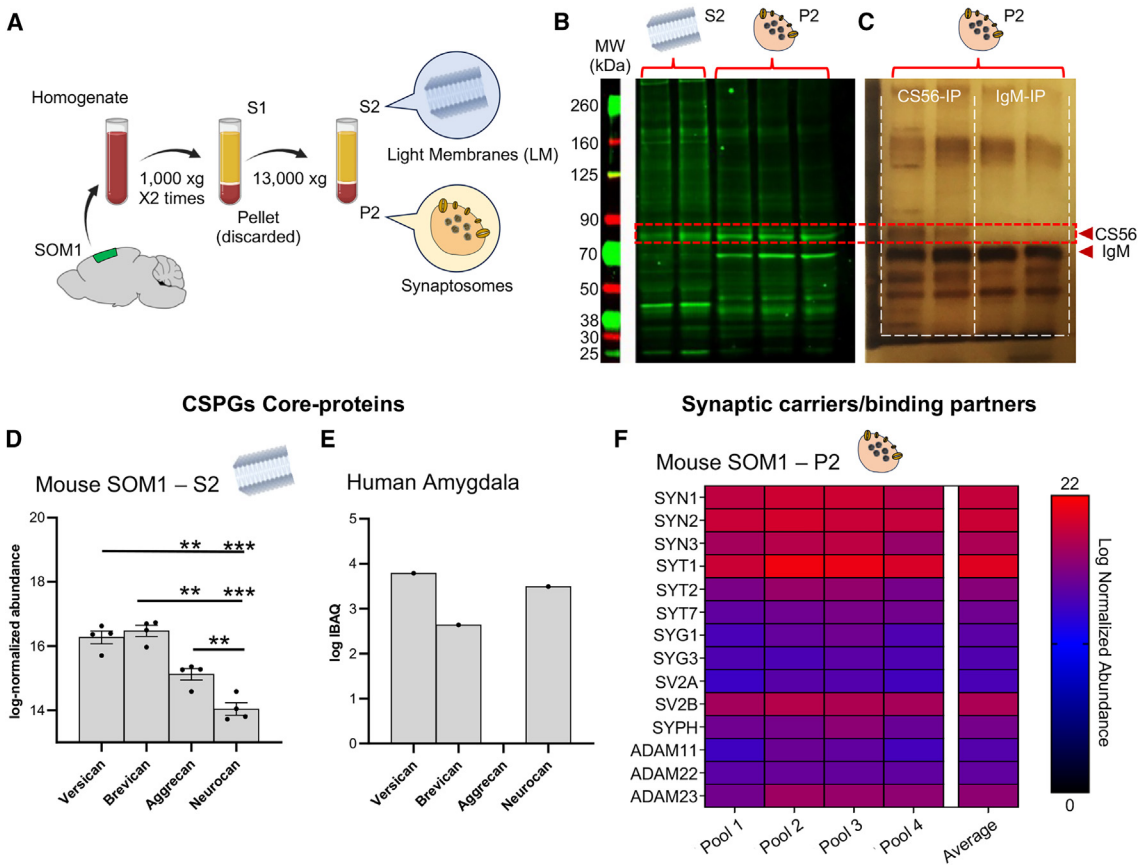

Figure 4. LC-MS/MS proteomic analysis of P2, containing crude synaptosomal fractions, suggests that CS56 may play a pivotal role in LTP

(A) Diagram describing the workflow for the preparation of samples to be analyzed with proteomics.

(B) Western blot of pre-IP protein lysates from the mouse primary somatosensory cortex showing a CS56-positive band at approximately 80 kDa molecular weight, in both S2 (containing the light membrane, left side) and P2 (containing crude synaptosomal fractions, right side).

(C) A representative picture of a gel colored with silver staining after CS56 IP confirms the specificity of the 80 kDa band. This band was excised from the gel and used for proteomics.

(D) Comparison between the log-normalized abundance of CSPG core proteins revealed a preferential association of Vcan and brevican with CS56. Vcan mean = 16.27, SEM = 0.19; brevican mean = 16.47, SEM = 0.17; aggrecan mean = 15.12, SEM = 0.18; neurocan mean = 14.04; SEM = 0.19. One-way ANOVA with Bonferroni correction for multiple comparisons, $n = 4$ pools of 4 mice per pool (16 total), two replicates per pool: Vcan vs. brevican $p > 0.999$, CI −0.5644 to 0.1591; Vcan vs. aggrecan $p = 0.005$, CI 0.7012 to 1.605; Vcan vs. neurocan $p < 0.0001$, CI 0.9390 to 3.527; brevican vs. aggrecan $p = 0.001$, CI 0.8954 to 1.816; brevican vs. neurocan $p < 0.0001$, CI 1.503 to 3.369; aggrecan vs. neurocan $p = 0.009$, CI −0.1207 to 2.281.

(E) Both Vcan and brevican, as well as neurocan, were found after CS56 IP in the human postmortem amygdala (the values shown represent two technical replicates on a single subject).

(F) Heatmap depicting the normalized abundance of synaptic plasticity-related proteins identified after CS56 IP from P2. The highest expression was found for synapsins and synaptotagmin-1. Note also the presence of ADA proteins, confirming CS56 as an ideal substrate for promoting activity-dependent remodeling of peri-synaptic ECM. (SYN, synapsins; SYT, synaptotagmins; SYG, synaptogyrins; SVT2, synaptic vesicle glycoproteins-2; SYPH, synaptophysin; ADA, disintegrin and metalloproteinase domain-containing proteins. Error bars indicate SEM. $^{**}p < 0.001$, $^{***}p < 0.0001$. SOM1, primary somatosensory cortex; S1, supernatant 1; S2, supernatant 2; P1, pellet 1; P2, pellet 2.

conclusions. With these findings, we establish that CS56-reactive CSPGs are a pleiotropic factor contributing to synaptic transmission, and we propose a direct role of CS56-recognized glycans in LTP induction via an AMPA-receptor-dependent mechanism.

CSPG Vcan regulates the expression of CS56-reactive glycans *in vivo*

Our proteomic findings highlight Vcan as one of the main core proteins bearing CS56 glycans. Interestingly, the co-expression of Vcan and CS56-reactive glycans had already been described in the mouse brain,[23] and Vcan was shown to regulate the expression of Chst7 in smooth muscle cells.[46] Hence, we decided to test whether CS56-labeled 6-sulfated chondroitin sulfate and Vcan are functionally related in the brain. First, we confirmed that Vcan and CSCs co-localize in both the BCx and the hippocampus of adult mice (Figures 5A, 5B, S8A, and S8B; Table S7). Then, we investigated the functional relationship between Vcan and CS56-reactive CSPGs by generating a Vcan RNA-interference construct (Vcan shRNA; Figure 5C). The

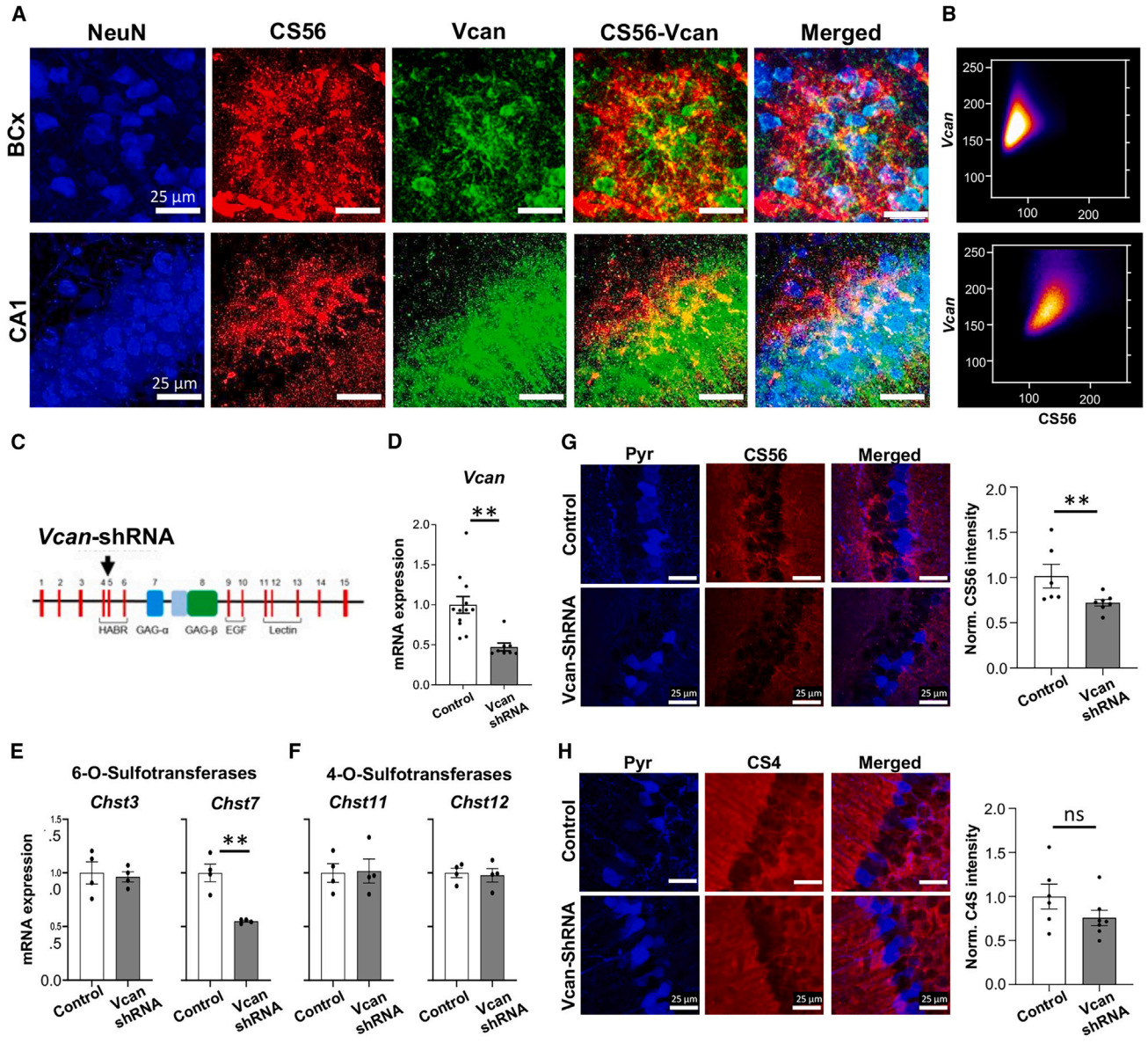

Figure 5. The expression of 6-sulfated chondroitin sulfate depends on the expression of the proteoglycan versican

(A) Representative photomicrograph showing CS56C co-localization with versican (Vcan) in both the BCx (top) and the CA1 hippocampal field (bottom). Scale bar, 25 µm.

(B) Representative scatterplot showing partial co-localization of Vcan and CS56 in BCx and CA1 in one representative photomicrograph. Mander's average co-localization coefficients: Vcan-CS56, BCx 0.491, CA1 0.497. CS56-Vcan, BCx 0.46, CA1 0.492. $n = 3$ mice.

(C) Diagram showing the site targeted by Vcan shRNA to downregulate Vcan expression.

(D) Vcan shRNA successfully knocks down Vcan in dissociated cultures. t test: control mean = 1, SEM = 0.1, $n = 8$; Vcan-shRNA mean = 0.47, SEM = 0.04, $n = 12$; $p < 0.0001$, CI −0.6254 to −0.2257.

(E and F) Vcan downregulation is paralleled by reduced expression of Chst7 6-O-sulfotransferase (E) and does not affect the expression of 4-O-sulfotransferases (Chst11 and 12) (F). t test: Vcan shRNA $n = 4$, controls $n = 4$. Chst3: control mean = 1, SEM = 0.1; Vcan shRNA mean = 0.96, SEM = 0.04; $p = 0.75$, CI −0.3132 to 0.2394. Chst7: control mean = 1, SEM = 0.08; Vcan shRNA mean = 0.54, SEM = 0.009; $p = 0.001$, CI −0.6517 to −0.2497. Chst11: control mean = 1, SEM = 0.08; Vcan shRNA mean = 1.01, SEM = 0.11; $p = 0.9$, CI −0.3302 to 0.3647. Chst12: control mean = 1, SEM = 0.04; Vcan shRNA mean = 0.97, SEM = 0.06; $p = 0.78$, CI −0.2107 to 0.1671.

(G and H) Vcan shRNA infusion downregulates CS56 expression in CA1 (G) but does not affect CS4 (H). Left: representative photomicrographs from the CA1 hippocampal region of one subject treated with control shRNA (top) or one treated with Vcan shRNA (bottom). Scale bar, 25 µm. Right: comparison of the mean fluorescence intensity for both CS56 (G) and CS4 (H). t test: controls $n = 6$, Vcan shRNA $n = 7$. CS56: control mean = 1.01, SEM = 0.13; Vcan shRNA mean = 0.72, SEM = 0.03; $p = 0.04$, CI −0.5738 to −0.01562. CS4: control mean = 1, SEM = 0.14; Vcan shRNA mean = 0.75, SEM = 0.08; $p = 0.15$, CI −0.5976 to 0.1113. Error bars indicate SEM. $^*p < 0.05$, $^{**}p < 0.001$.

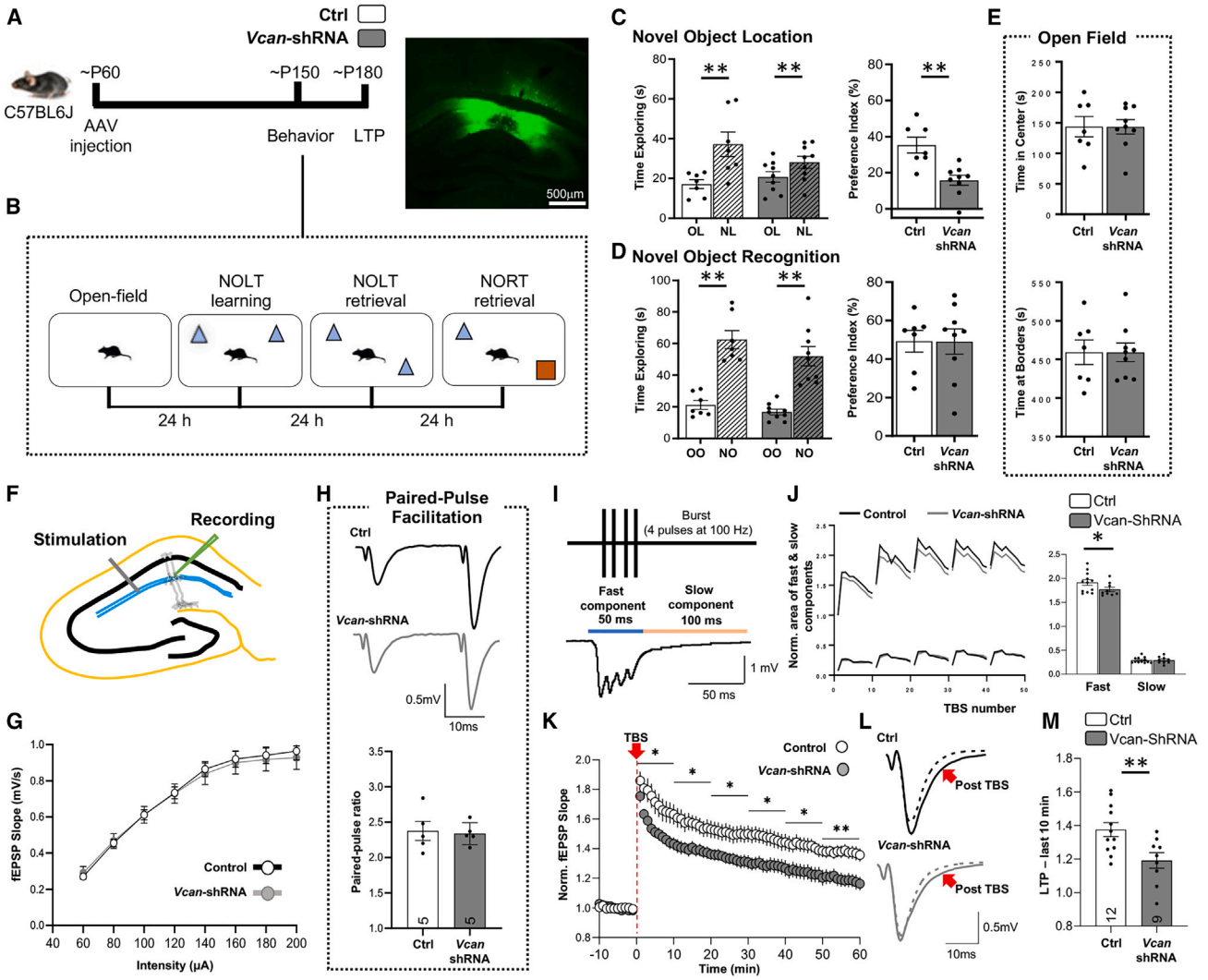

Figure 6. Vcan downregulation impairs hippocampal-dependent memory and CA1 LTP

(A) Schematic view of the experimental timeline. Scale bar, 500 µm.

(B) Graphical representation of the behavioral test experimental design.

(C–E) $n = 7$ for control mice (white and shaded white bars) and $n = 9$ for Vcan shRNA mice (gray and shaded bars). OL, old location; NL, new location; OO, old object; NO, new object. (C) During the recall session, both groups of mice treated with control or Vcan shRNA showed a preference for the novel location; paired t test: control, OL mean = 17.16, SEM = 2.22; NL mean = 37.2, SEM = 6.16; $p = 0.006$, CI 8.116 to 31.97; Vcan shRNA, OL mean = 20.78, SEM = 2.64; NL mean = 28.17, SEM = 3.03; $p = 0.001$, CI 4.010 to 10.77, but the preference index significantly decreased after Vcan knockdown. Preference index: Mann-Whitney test, control mean = 35.3, SEM = 4.4; Vcan shRNA mean = 15.78, SEM = 2.78; $p = 0.001$, CI −30.86 to −7.887. (D) New object preference in the NORT was unaffected in Vcan-shRNA-treated mice compared to controls; paired t test: control, OO mean = 21.17, SEM = 2.22; NO mean = 62.47, SEM = 5.75; $p < 0.001$, CI 26.03 to 56.57; Vcan shRNA, OO mean = 16.73, SEM = 1.78; NO mean = 52, SEM = 6.11; $p < 0.001$, CI 19.49 to 51.05. Preference index: Mann-Whitney test, control mean = 49.23, SEM = 5.63; Vcan shRNA mean = 49.03, SEM = 6.57; $p > 0.99$, CI −16.40 to 19.73. (E) Vcan knockdown does not affect the basic locomotor activity or generalized anxiety in the open field; t test: time center, controls mean = 143.7, SEM = 16.51; Vcan shRNA mean = 43.3, SEM = 11.97; $p = 0.098$, CI −43.01 to 42.20. t test: time borders, controls mean = 459.2, SEM = 15.87; Vcan shRNA mean = 459.1, SEM = 11.93; $p = 0.099$, CI −41.78 to 41.59.

(F) Diagram showing the location of stimulation and recording sites in the hippocampus used in the *ex vivo* experiments.

(G) The input/output curve shows no difference in the fEPSPs of mice treated with Vcan shRNA compared to the control; repeated-measures two-way ANOVA $p = 0.8369$, CI −0.1097 to 0.1340.

(H) Paired-pulse facilitation is unaffected by Vcan shRNA treatment; t test: control mean = 2.37, SEM = 0.13, $n = 5$ slices from three animals; Vcan shRNA mean = 2.33, SEM = 0.06, $n = 5$ slices from three animals, $p = 0.8083$, CI −0.3873 to 0.3113.

(I) A scheme showing the time windows used for measurements of the fast (predominantly AMPA receptor mediated) and slow (predominantly NMDA receptor mediated) components of theta-burst-induced fEPSPs.

(J) Reduction in potentiation of the fast and no changes in the slow component after Vcan knockdown. Mann-Whitney test: fast, control mean = 1.91, SEM = 0.06; Vcan shRNA mean = 1.76, SEM = 0.04; $p = 0.049$, CI −0.2957 to −0.001388. Slow: control mean = 0.29, SEM = 0.01; Vcan shRNA mean = 0.29, SEM = 0.02; $p > 0.99$, CI −0.05976 to 0.06310.

(legend continued on next page)

construct was first tested in mouse dissociated hippocampal cultures, where it successfully reduced Vcan mRNA expression by >50% (Figure 5D). Importantly, downregulation of Vcan was accompanied by a significant and selective decrease in Chst7 mRNA expression (Figure 5E), without affecting chondroitin-4-O-sulfotransferase mRNAs (Figure 5F). To confirm these findings *in vivo*, we injected our construct in the CA1 hippocampal subregion of adult mice. Consistent with *in vitro* findings, we found that Vcan shRNA infusion induced a significant and correlated decrease in both Vcan and CS56 in this area (Figures 5G and S8C–S8E). Expression of CS4, conversely, was not affected (Figure 5H). These findings confirmed that Vcan and CS56-reactive glycans are functionally related, putatively contributing to the same biological function, and provided a tool to selectively downregulate the expression CS56-reactive CSPGs *in vivo* targeting one of its main carriers.

Vcan contributes to hippocampal-dependent synaptic plasticity and memory

After demonstrating the functional association between CS56-reactive CSPGs and Vcan, we proceeded to test the hypothesis that Vcan might actively contribute to learning and memory consolidation via an LTP-dependent mechanism. To do so, we shifted our focus to the CA1 hippocampal region, where object-location learning tasks can be used as a behavioral readout for locally determined LTP-dependent learning.[47,48] Mice were injected with control or Vcan shRNA at 2 months of age and tested for both hippocampal-dependent and independent memory 3 months later (Figures 6A and 6B). Afterward, animals were sacrificed to assess hippocampal LTP in acute slices (Figure 6A). In line with our expectations, mice treated with Vcan shRNA showed selective impairment in CA1-dependent memory in a novel object location test (Figure 6C),[49] while peri-rhinal cortex-dependent object recognition was unaffected (Figure 6D).[50] No changes in locomotor activity or anxiety could be detected in the open field in Vcan-shRNA-treated mice (Figure 6E). We then assessed whether this impairment in hippocampal-dependent memory was associated with a deficit in hippocampal LTP, recording local field potentials in acute slices (Figure 6F). First, we established that Vcan shRNA affects neither the basal excitatory transmission (Figure 6G) nor paired-pulse facilitation, a form of pre-synaptic short-term plasticity (Figure 6H). To induce LTP, we used theta-burst stimulation (TBS) as a learning-relevant pattern of high-frequency synaptic stimulation (Figure 6I). During TBS (Figure 6I), the fast component of field excitatory post-synaptic potentials (fEPSPs), predominantly mediated by AMPA receptors, was increased less prominently in slices from Vcan shRNA mice compared to controls, while the slow component, predominantly mediated by NMDA receptors, was not affected (Figure 6J). After TBS, we observed impaired LTP in mice treated with Vcan shRNA at every 10 min interval up to 1 h post-induction (Figures 6K–6M). Impaired potentiation of synaptic responses during and immediately after TBS suggests the role of Vcan in the induction of LTP. Altogether, these findings corroborate our hypothesis showing that 6-sulfated CSPG Vcan is a critical component of the molecular machinery underlying activity-dependent changes in synaptic strength, and it is required for learning and memory.

DISCUSSION

In this work, we show that ECM structures, composed of 6-sulfated CSPGs, present temporal, molecular (ARC), and subcellular (spine geometry) features consistent with the dynamics of local synaptic remodeling. Specifically, the converging accumulation of CS56 immunoreactivities in glial cell processes and into the peri-synaptic space (Figure 1) led us to postulate that the morphological conformation of CSCs might correspond to a snapshot of a transient biological process of coordinated multi-synaptic plasticity. To test this hypothesis, we analyzed dendritic spine geometry as a proxy for synaptic efficacy, showing that the population of spines contained within CSCs presents striking morphological homogeneity compared to synapses located outside (Figure 2G). In particular, we show that the early phase CSCs (R-CSCs) predominantly associate with larger, putatively potentiated, dendritic spines (Figure 3A), while D-CSCs present marginally decreased synaptic size (Figure 3B). Accordingly, D-CSCs were found preferentially associated with dendritic expression of the neuroplastic protein ARC, which is known to reach synaptic targets approximately 2 h after a triggering stimulus to drive heterosynaptic depression during locally coordinated synaptic clustering[4,7] (Figure 3). Then, we used complementary approaches of sensory deprivation and stimulation to show that CSCs arise in response to sensory experience, presenting a distinctive morphological appearance depending on the time delay from the triggering stimulus (i.e., 1 h for R-CSCs, 2 h for D-CSCs, Figure 2).

In line with this evidence, we postulate a working model (summarized in Figure 7) where 6-sulfated chondroitin sulfate plays an active role in the acute phase of local synaptic remodeling. According to this model, when LTP is induced, CS56-reactive CSPGs accumulate in glial cells, giving rise to the characteristic rosette shape of R-CSCs. Then, CSPGs are released by glia through their endfeet and incorporated into the peri-synaptic space. Thus, in our view, R-CSCs are predominantly distinguishable during the rising phase of s-LTP. Finally, when the local s-LTP reaches its plateauing phase, CSPGs' peri-synaptic accumulation reaches a saturation point, resulting in the distinct dense punctate morphology of D-CSCs, coincident with the dendritic accumulation of ARC protein. At this point, a broad-scale selection is triggered by the endocytotic action of ARC,[4,7] resulting in the targeted maintenance of a small

(K) TBS-induced synaptic potentiation is impaired by Vcan shRNA treatment in all 10 min intervals after TBS; repeated-measures two-way ANOVA, Fisher's LSD *post hoc* analysis, $p = 0.0196$, CI 0.02769 to 0.2816.

(L) Representative traces showing changes in the fEPSP slope before (dashed line) and after (solid line) TBS, for control (top) and Vcan-shRNA-treated (bottom) mice.

(M) LTP is significantly impaired by Vcan shRNA treatment 50–60 min after TBS; t test: control mean = 1.37, SEM = 0.04, $n = 12$ slices from five mice; Vcan shRNA mean = 1.19, SEM = 0.04, $n = 9$ slices from six mice, $p = 0.0086$, CI −0.3155 to −0.05246. Error bars indicate SEM. $^{*}p < 0.05$, $^{**}p < 0.001$, $^{***}p < 0.0001$.

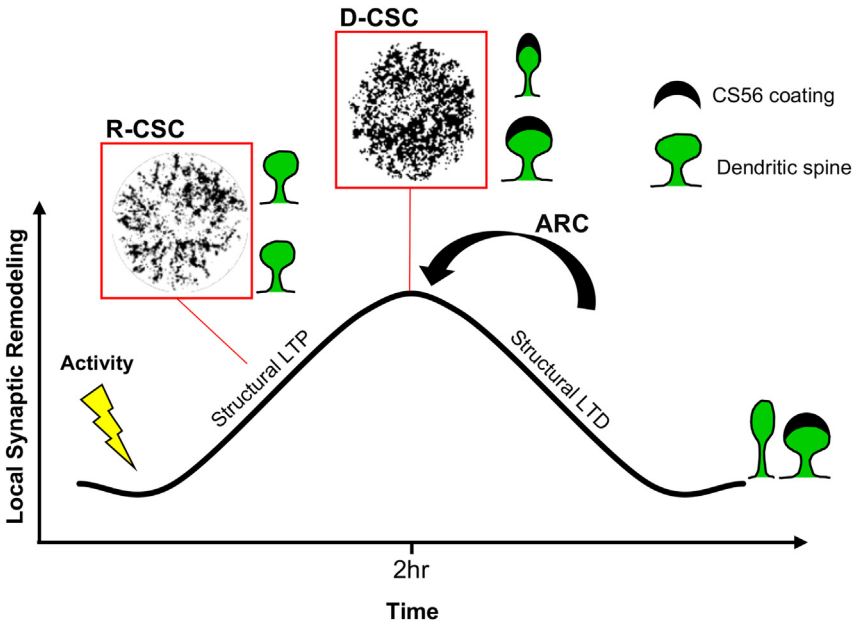

Figure 7. Model of CSC dynamics associated with localized synaptic plasticity

We propose that CSCs are transient structures involved in regulating multi-synaptic, activity-dependent plasticity within a segregated space. Our evidence suggests that R-CSCs emerge during the rising phase of s-LTP, characterized by significantly increased synaptic size and accumulation of converging CS56-IR glial processes. D-CSCs, in contrast, show a decrease in synaptic size as well as spatiotemporal association with ARC protein, suggesting that they might correspond to the inversion phase of local structural plasticity and the beginning of the s-LTD.

percentage of the originally potentiated terminals.[6] We speculate that these stably preserved synapses may retain CS56 coating beyond the temporal limits of CSC manifestation, putatively accounting for the sparse CS56 punctum labeling that is observed outside of CSCs (Figures 1B and 1D).

To investigate the role of CS56-reactive CSPGs in the synaptic machinery, we co-immunoprecipitated its binding partners from crude synaptosomal fractions (Figure 4). We found that CS56 robustly associates with proteins required for the induction of AMPA-receptor-dependent LTP, suggesting that this specific CSPG glycoform directly contributes to activity-dependent plasticity by promoting synaptic vesicle trafficking. To test this hypothesis, we successfully downregulated CS56 by knocking down its carrier Vcan (Figure 5). With this strategy, we were able to show that selective downregulation of 6-sulfated Vcan impairs the induction of hippocampal LTP and hippocampus-dependent memory (Figure 6). Interestingly, LTP was not completely abolished but significantly reduced by Vcan depletion, affecting AMPA-receptor-mediated responses selectively. This observation agrees with the outcomes of a previous work showing that the upregulation of CSPG Vcan was seen in the hippocampus of animals trained in the Morris water maze, and Vcan was found to co-precipitate with the glutamate receptor 1 subunit of AMPA receptors. Peri-synaptic ECM has been previously shown to regulate lateral diffusion of AMPA receptors in principal neurons.[8] Thus, AMPA receptors inserted into the membrane after induction of LTP may not rapidly diffuse away from synapses due to peri-synaptic ECM barriers and, hence, have more chances to be properly integrated into the post-synaptic density. This mechanism may be particularly important during the consolidation phase, when most essential recent sensory information is replayed and integrated with existing information. In addition, the endocytosis of peri-synaptic ECM molecules[51] may also be linked to the endocytosis of associated AMPA receptors. This evidence, in line with previous work, highlights the role of 6-sulfated CSPGs in promoting a dynamic extracellular environment, permissive for synaptic modifications,[21–23] and suggests that ECM molecules shape both the induction of synaptic plasticity and the long-term stabilization of newly potentiated synapses. Furthermore, by showing remarkable similarities with recent understanding in the field of activity-dependent dynamics of dendritic spines,[1,3–6,34] our findings successfully integrate current knowledge, suggesting that the chemical composition of the brain ECM is pivotal in acutely mediating synaptic structural and functional refinement.[11,21,22]

Importantly, our findings have direct translational relevance. Previous work described a significant reduction of CSCs in the postmortem brain of people with schizophrenia and bipolar disorder,[26] aligning with a body of evidence showing multiple alterations in the brain ECM components in psychiatric disorders.[10,26,27,52,53] By demonstrating a direct role of CS56-reactive CSPGs in LTP, we reconcile the emergent role of the brain ECM in the neuropathology of psychiatric illnesses with well-established evidence of altered structural plasticity, which is considered a critical neuropathological hallmark in these conditions.[54,55] It will be crucial, in future studies, to address how alteration of ECM molecules impacts synaptic plasticity in the context of schizophrenia and bipolar disorder; it will also be important to understand how impairment of synaptic plasticity may contribute to the loss of ECM components in these disorders.

Finally, an intriguing speculation comes from the conspicuous geometrical shape of CSCs, which we have shown to be well conserved across mammalian species. Given the convergence of our findings, it is reasonable to think that synaptic terminals incorporated within CSCs might be concomitantly affected by the same triggering event. Thus, CSCs might highlight locally segregated synaptic ensembles undergoing parallel and coordinated phenomena of homo- and heterosynaptic plasticity. Should this hypothesis be verified by future studies, CSCs could be exploited as a valuable tool in the hands of neuroscientists to visually identify a cluster of locally coordinated and functionally heterogeneous synapses during the active phase of plastic remodeling. Furthermore, this finding would suggest that activity-dependent synaptic refinement occurs within segregated microenvironments, corroborating empirical evidence showing

that spatially organized microcircuits represent ideally functional computational units to integrate sensory information and fulfill complex biological functions.[1,2]

Taken together, these studies provide evidence for the role of CSPGs in spatially coordinated plasticity. They support the hypothesis that CSCs are transient structures involved in regulating multi-synaptic plasticity within a segregated space (Figure 7), potentially contributing to the interaction between glial cells, ECM, and synaptic elements during the active phase of local synaptic refinement.

Limitations of the study

Viable tools to track and visualize CSPG post-translational modifications in live and behaving animals are not currently available. Thus, it was not possible to provide a complete account of the temporal dynamics driving CSCs. For instance, it was not possible to show CSC formation in the hippocampus during memory acquisition. We hope that this study will motivate future research in this regard. Another limitation is that only males were included in this study in order to optimize data collection and analysis. Although previous studies do not suggest significant sex differences in the expression of CSCs,[25,26] future studies will investigate potential sex differences.

We recognize a gap in our data. On one hand, we show that CS56-reactive CSPGs are putatively derived from glial cells during the active phase of synaptic remodeling. On the other hand, we show that Vcan and CS56-reactive CSPGs are required for LTP induction. Given that it is unlikely for glial cells to secrete CSPGs faster than the time required for synaptic vesicle docking during high-frequency stimulation, we must consider the possibility that CSCs may not contribute to the induction of LTP directly. One possibility is that CSPGs are permanently stored within glial cell processes and quickly glycosylated and secreted in concomitance with neurotransmitter release. This would allow CS56 to bind synaptic proteins within the synaptic cleft, facilitating pre-post synaptic communication and the induction of LTP. One fascinating alternative interpretation could be that when a first stimulus pervades a synaptic ensemble, CS56-reactive CSPGs are mobilized and form a CSC as a preparatory substrate receptive to additional stimuli. When the next stimulus reaches the same ensemble, the CSC's geographical arrangement selectively facilitates the induction of LTP onto 6-sulfated CSPG-coated terminals, thus maximizing the efficacy of memory consolidation supported by repetitive exposure to the same stimulus.

In either case, our work shows that 6-sulfated CSPGs are critical mediators of activity-dependent plasticity, highlighting the need for better tools to study CSPG glycoforms as critical mediators of learning, memory, and brain circuit refinement.

STAR★METHODS

Detailed methods are provided in the online version of this paper and include the following:

SUPPLEMENTAL INFORMATION

Supplemental information can be found online at https://doi.org/10.1016/j.celrep.2024.114112.

ACKNOWLEDGMENTS

G.C. was supported by the Rappaport mental health research fellowship 2018–2019 (https://rappaportfoundation.org/fellow/gabriele-chelini-phd/) and the CARITRO postdoctoral research fellowship 2021–2023 (https://www.fondazionecaritro.it/bandi/bando-post-doc-2021/). L.B. was supported by a PhD fellowship of the Caritro Foundation (Trento, Italy). We thank Rahul Kaushik for the valuable discussion and Katrin Boehm for the production and purification of AAVs. Y.B. was supported by the TRAIN – Trentino Autism Initiative, a 2018–2022 strategic project of the University of Trento, Italy. This work has been supported by DAAD (fellowship to D.B.-A.) and the Deutsche Forschungsgemeinschaft (DFG; German Research Foundation), Project-ID 362321501/RTG 2413 SynAGE and 425899996/SFB 1436 subproject A05 (to A.D.). S.B. was supported by NIH R01MH104488 and NIH R01MH120991; T.K. was supported by NIH R21HD088931, R21HD097524, R21MH117609, and R01HD102974; R.M. was supported by NIMH R01 MH107487 and MH121102; and K.J.R. was supported by NIH R01 MH108665 and MH120991 and NIH P50 MH115874.

The graphical contents composing Figure 4A were legally acquired from https://it.dreamstime.com/ and biorender.com and readapted for the figure.

AUTHOR CONTRIBUTIONS

G.C. contributed to the conceptualization of the project, carried out most of the research work, provided funding, and wrote the manuscript. H.M. carried out viral injection, electrophysiology, quantitative PCR analysis, immunohistochemistry, and image analysis and wrote the draft version of the manuscript for these experiments. P.D. contributed to data collection and analyses. D.B.-A. did behavioral experiments and immunohistochemistry. S.M.O'D. and J.Z. carried out proteomics studies in the mouse. S.M.O'D. and R.M. carried out proteomics studies in human postmortem tissue. T.K. contributed to manuscript preparation. L.B. and Y.B. performed sensory stimulation experiments. Y.B. provided funding and contributed to manuscript preparation. C.B. carried out the electron microscopy work. A.B.-B. contributed to most of the research work. K.J.R. provided resources and contributed to the manuscript preparation. A.D. contributed to the conceptualization of the work and its supervision, provided resources for learning and memory and electrophysiology experiments, and contributed to manuscript preparation. S.B. contributed to the conceptualization of the project and its supervision, data analysis, resources, and manuscript preparation. A.D., Y.B., and S.B. equally supervised manuscript preparation.

DECLARATION OF INTERESTS

The authors declare no competing interests.

Received: July 10, 2023
Revised: November 9, 2023
Accepted: March 28, 2024

REFERENCES

1. Kastellakis, G., and Poirazi, P. (2019). Synaptic clustering and memory formation. Front. Mol. Neurosci. *12*, 300. https://doi.org/10.3389/fnmol.2019.00300.
2. Caroni, P., Donato, F., and Muller, D. (2012). Structural plasticity upon learning: regulation and functions. Nat. Rev. Neurosci. *13*, 478–490. https://doi.org/10.1038/nrn3258.
3. Govindarajan, A., Israely, I., Huang, S.-Y., and Tonegawa, S. (2011). The dendritic branch is the preferred integrative unit for protein synthesis-dependent LTP. Neuron *69*, 132–146. https://doi.org/10.1016/j.neuron.2010.12.008.
4. El-Boustani, S., Ip, J.P.K., Breton-Provencher, V., Knott, G.W., Okuno, H., Bito, H., and Sur, M. (2018). Locally coordinated synaptic plasticity of visual cortex neurons in vivo. Science *360*, 1349–1354. https://doi.org/10.1126/science.aao0862.
5. Jenks, K.R., Tsimring, K., Ip, J.P.K., Zepeda, J.C., and Sur, M. (2021). heterosynaptic plasticity and the experience-dependent refinement of developing neuronal circuits. Front. Neural Circuits *15*, 803401. https://doi.org/10.3389/fncir.2021.803401.
6. Yang, G., Pan, F., and Gan, W.-B. (2009). Stably maintained dendritic spines are associated with lifelong memories. Nature *462*, 920–924. https://doi.org/10.1038/nature08577.
7. Okuno, H., Akashi, K., Ishii, Y., Yagishita-Kyo, N., Suzuki, K., Nonaka, M., Kawashima, T., Fujii, H., Takemoto-Kimura, S., Abe, M., et al. (2012). Inverse synaptic tagging of inactive synapses via dynamic interaction of Arc/Arg3.1 with CaMKIIβ. Cell *149*, 886–898. https://doi.org/10.1016/j.cell.2012.02.062.
8. Frischknecht, R., Heine, M., Perrais, D., Seidenbecher, C.I., Choquet, D., and Gundelfinger, E.D. (2009). Brain extracellular matrix affects AMPA receptor lateral mobility and short-term synaptic plasticity. Nat. Neurosci. *12*, 897–904. https://doi.org/10.1038/nn.2338.
9. Dityatev, A., Seidenbecher, C.I., and Schachner, M. (2010). Compartmentalization from the outside: the extracellular matrix and functional microdomains in the brain. Trends Neurosci. *33*, 503–512. https://doi.org/10.1016/j.tins.2010.08.003.
10. Chelini, G., Pantazopoulos, H., Durning, P., and Berretta, S. (2018). The tetrapartite synapse: a key concept in the pathophysiology of schizophrenia. Eur. Psychiatry. *50*, 60–69. https://doi.org/10.1016/j.eurpsy.2018.02.003.
11. Foscarin, S., Raha-Chowdhury, R., Fawcett, J.W., and Kwok, J.C.F. (2017). Brain ageing changes proteoglycan sulfation, rendering perineuronal nets more inhibitory. Aging *9*, 1607–1622. https://doi.org/10.18632/aging.101256.
12. Sorg, B.A., Berretta, S., Blacktop, J.M., Fawcett, J.W., Kitagawa, H., Kwok, J.C.F., and Miquel, M. (2016). Casting a wide net: role of perineuronal nets in neural plasticity. J. Neurosci. *36*, 11459–11468. https://doi.org/10.1523/JNEUROSCI.2351-16.2016.
13. Miller, G.M., and Hsieh-Wilson, L.C. (2015). Sugar-dependent modulation of neuronal development, regeneration, and plasticity by chondroitin sulfate proteoglycans. Exp. Neurol. *274*, 115–125. https://doi.org/10.1016/j.expneurol.2015.08.015.
14. De Vivo, L., Landi, S., Panniello, M., Baroncelli, L., Chierzi, S., Mariotti, L., Spolidoro, M., Pizzorusso, T., Maffei, L., and Ratto, G.M. (2013). Extracellular matrix inhibits structural and functional plasticity of dendritic spines in the adult visual cortex. Nat. Commun. *4*, 1484. https://doi.org/10.1038/ncomms2491.
15. Orlando, C., Ster, J., Gerber, U., Fawcett, J.W., and Raineteau, O. (2012). Perisynaptic chondroitin sulfate proteoglycans restrict structural plasticity in an integrin-dependent manner. J. Neurosci. *32*, 18009–18017. https://doi.org/10.1523/JNEUROSCI.2406-12.2012.
16. Senkov, O., Andjus, P., Radenovic, L., Soriano, E., and Dityatev, A. (2014). Neural ECM molecules in synaptic plasticity, learning, and memory. In Progress in Brain Research, A. Dityatev, B. Wehrle-Haller, and A. Pitkänen, eds. (Elsevier), pp. 53–80. https://doi.org/10.1016/B978-0-444-63486-3.00003-7.
17. Pizzorusso, T., Medini, P., Berardi, N., Chierzi, S., Fawcett, J.W., and Maffei, L. (2002). Reactivation of ocular dominance plasticity in the adult visual cortex. Science *298*, 1248–1251. https://doi.org/10.1126/science.1072699.
18. Banerjee, S.B., Gutzeit, V.A., Baman, J., Aoued, H.S., Doshi, N.K., Liu, R.C., and Ressler, K.J. (2017). Perineuronal nets in the adult sensory cortex are necessary for fear learning. Neuron *95*, 169–179.e3. https://doi.org/10.1016/j.neuron.2017.06.007.
19. Gogolla, N., Caroni, P., Lüthi, A., and Herry, C. (2009). Perineuronal nets protect fear memories from erasure. Science *325*, 1258–1261. https://doi.org/10.1126/science.1174146.
20. Ramsaran, A.I., Wang, Y., Golbabaei, A., Aleshin, S., de Snoo, M.L., Yeung, B.A., Rashid, A.J., Awasthi, A., Lau, J., Tran, L.M., et al. (2023). A shift in the mechanisms controlling hippocampal engram formation during brain maturation. Science *380*, 543–551.
21. Yang, S., Gigout, S., Molinaro, A., Naito-Matsui, Y., Hilton, S., Foscarin, S., Nieuwenhuis, B., Tan, C.L., Verhaagen, J., Pizzorusso, T., et al. (2021). Chondroitin 6-sulphate is required for neuroplasticity and memory in ageing. Mol. Psychiatry *26*, 5658–5668. https://doi.org/10.1038/s41380-021-01208-9.
22. Miyata, S., Komatsu, Y., Yoshimura, Y., Taya, C., and Kitagawa, H. (2012). Persistent cortical plasticity by upregulation of chondroitin 6-sulfation. Nat. Neurosci. *15*, 414–S2. https://doi.org/10.1038/nn.3023.
23. Baidoe-Ansah, D., Sakib, S., Jia, S., Mirzapourdelavar, H., Strackeljan, L., Fischer, A., Aleshin, S., Kaushik, R., and Dityatev, A. (2022). Aging-associated changes in cognition, expression and epigenetic regulation of chondroitin 6-sulfotransferase Chst3. Cells *11*, 2033. https://doi.org/10.3390/cells11132033.
24. Deepa, S.S., Yamada, S., Fukui, S., and Sugahara, K. (2007). Structural determination of novel sulfated octasaccharides isolated from chondroitin sulfate of shark cartilage and their application for characterizing monoclonal antibody epitopes. Glycobiology *17*, 631–645. https://doi.org/10.1093/glycob/cwm021.
25. Hayashi, N., Tatsumi, K., Okuda, H., Yoshikawa, M., Ishizaka, S., Miyata, S., Manabe, T., and Wanaka, A. (2007). DACS, novel matrix structure composed of chondroitin sulfate proteoglycan in the brain. Biochem. Biophys. Res. Commun. *364*, 410–415. https://doi.org/10.1016/j.bbrc.2007.10.040.
26. Pantazopoulos, H., Markota, M., Jaquet, F., Ghosh, D., Wallin, A., Santos, A., Caterson, B., and Berretta, S. (2015). Aggrecan and chondroitin-6-sulfate abnormalities in schizophrenia and bipolar disorder: a postmortem study on the amygdala. Transl. Psychiatry *5*, e496. https://doi.org/10.1038/tp.2014.128.
27. Matuszko, G., Curreli, S., Kaushik, R., Becker, A., and Dityatev, A. (2017). Extracellular matrix alterations in the ketamine model of schizophrenia. Neuroscience *350*, 13–22. https://doi.org/10.1016/j.neuroscience.2017.03.010.
28. Jasnow, A.M., Ehrlich, D.E., Choi, D.C., Dabrowska, J., Bowers, M.E., McCullough, K.M., Rainnie, D.G., and Ressler, K.J. (2013). Thy1-expressing neurons in the basolateral amygdala may mediate fear inhibition. J. Neurosci. *33*, 10396–10404. https://doi.org/10.1523/JNEUROSCI.5539-12.2013.

29. Gray, E.G. (1959). Axo-somatic and axo-dendritic synapses of the cerebral cortex: an electron microscope study. J. Anat. *93*, 420–433.

30. Harris, K.M., and Weinberg, R.J. (2012). ultrastructure of synapses in the mammalian brain. Cold Spring Harb. Perspect. Biol. *4*, a005587. https://doi.org/10.1101/cshperspect.a005587.

31. Saunders, A., Macosko, E.Z., Wysoker, A., Goldman, M., Krienen, F.M., De Rivera, H., Bien, E., Baum, M., Bortolin, L., Wang, S., et al. (2018). Molecular diversity and specializations among the cells of the adult mouse brain. Cell *174*, 1015–1030.e16. https://doi.org/10.1016/j.cell.2018.07.028.

32. Harris, K.M., and Stevens, J.K. (1989). Dendritic spines of CA 1 pyramidal cells in the rat hippocampus: serial electron microscopy with reference to their biophysical characteristics. J. Neurosci. *9*, 2982–2997. https://doi.org/10.1523/JNEUROSCI.09-08-02982.1989.

33. Noguchi, J., Nagaoka, A., Watanabe, S., Ellis-Davies, G.C.R., Kitamura, K., Kano, M., Matsuzaki, M., and Kasai, H. (2011). *In vivo* two-photon uncaging of glutamate revealing the structure-function relationships of dendritic spines in the neocortex of adult mice: *In vivo* two-photon glutamate uncaging. J. Physiol. *589*, 2447–2457. https://doi.org/10.1113/jphysiol.2011.207100.

34. Bosch, M., and Hayashi, Y. (2012). Structural plasticity of dendritic spines. Curr. Opin. Neurobiol. *22*, 383–388. https://doi.org/10.1016/j.conb.2011.09.002.

35. Balasco, L., Pagani, M., Pangrazzi, L., Chelini, G., Ciancone Chama, A.G., Shlosman, E., Mattioni, L., Galbusera, A., Iurilli, G., Provenzano, G., et al. (2022). Abnormal whisker-dependent behaviors and altered cortico-hippocampal connectivity in *Shank3b* −/− mice. Cereb. Cortex *32*, 3042–3056. https://doi.org/10.1093/cercor/bhab399.

36. Ghazanfar, A.A., and Nicolelis, M.A. (1999). Spatiotemporal Properties of Layer V Neurons of the Rat Primary Somatosensory Cortex. Cereb. Cortex *9*, 348–361. https://doi.org/10.1093/cercor/9.4.348.

37. Ramirez, A., Pnevmatikakis, E.A., Merel, J., Paninski, L., Miller, K.D., and Bruno, R.M. (2014). Spatiotemporal receptive fields of barrel cortex revealed by reverse correlation of synaptic input. Nat. Neurosci. *17*, 866–875. https://doi.org/10.1038/nn.3720.

38. Wirths, O. (2017). Preparation of crude synaptosomal fractions from mouse brains and spinal Cords. Bio. Protoc. *7*, e2423. https://doi.org/10.21769/BioProtoc.2423.

39. Madrigal, M.P., Portalés, A., SanJuan, M.P., and Jurado, S. (2019). Postsynaptic SNARE proteins: role in synaptic transmission and plasticity. Neuroscience *420*, 12–21. https://doi.org/10.1016/j.neuroscience.2018.11.012.

40. Kittel, R.J., and Heckmann, M. (2016). Synaptic vesicle proteins and active zone plasticity. Front. Synaptic Neurosci. *8*, 8. https://doi.org/10.3389/fnsyn.2016.00008.

41. Wu, D., Bacaj, T., Morishita, W., Goswami, D., Arendt, K.L., Xu, W., Chen, L., Malenka, R.C., and Südhof, T.C. (2017). Postsynaptic synaptotagmins mediate AMPA receptor exocytosis during LTP. Nature *544*, 316–321. https://doi.org/10.1038/nature21720.

42. Janz, R., Südhof, T.C., Hammer, R.E., Unni, V., Siegelbaum, S.A., and Bolshakov, V.Y. (1999). essential roles in synaptic plasticity for Synaptogyrin I and Synaptophysin I. Neuron *24*, 687–700. https://doi.org/10.1016/S0896-6273(00)81122-8.

43. Stout, K.A., Dunn, A.R., Hoffman, C., and Miller, G.W. (2019). the synaptic vesicle glycoprotein 2: structure, function, and disease relevance. ACS Chem. Neurosci. *10*, 3927–3938. https://doi.org/10.1021/acschemneuro.9b00351.

44. Cesca, F., Baldelli, P., Valtorta, F., and Benfenati, F. (2010). The synapsins: key actors of synapse function and plasticity. Prog. Neurobiol. *91*, 313–348. https://doi.org/10.1016/j.pneurobio.2010.04.006.

45. Peters, J.J., Leitz, J., Oses-Prieto, J.A., Burlingame, A.L., and Brunger, A.T. (2021). Molecular characterization of AMPA-receptor-containing vesicles. Front. Mol. Neurosci. *14*, 754631. https://doi.org/10.3389/fnmol.2021.754631.

46. Keire, P.A., Bressler, S.L., Mulvihill, E.R., Starcher, B.C., Kang, I., and Wight, T.N. (2016). Inhibition of versican expression by siRNA facilitates tropoelastin synthesis and elastic fiber formation by human SK-LMS-1 leiomyosarcoma smooth muscle cells in vitro and in vivo. Matrix Biol. *50*, 67–81. https://doi.org/10.1016/j.matbio.2015.12.010.

47. Cinalli, D.A., Cohen, S.J., Calubag, M., Oz, G., Zhou, L., and Stackman, R.W. (2023). DREADD -inactivation of dorsal CA1 pyramidal neurons in mice impairs retrieval of object and spatial memories. Hippocampus *33*, 6–17. https://doi.org/10.1002/hipo.23484.

48. Ásgeirsdóttir, H.N., Cohen, S.J., and Stackman, R.W. (2020). Object and place information processing by CA1 hippocampal neurons of C57BL/6J mice. J. Neurophysiol. *123*, 1247–1264. https://doi.org/10.1152/jn.00278.2019.

49. Donato, F., Alberini, C.M., Amso, D., Dragoi, G., Dranovsky, A., and Newcombe, N.S. (2021). The ontogeny of hippocampus-dependent memories. J. Neurosci. *41*, 920–926. https://doi.org/10.1523/JNEUROSCI.1651-20.2020.

50. Jo, Y.S., and Lee, I. (2010). Disconnection of the hippocampal-perirhinal cortical circuits severely disrupts object-place paired associative memory. J. Neurosci. *30*, 9850–9858. https://doi.org/10.1523/JNEUROSCI.1580-10.2010.

51. Dankovich, T.M., Kaushik, R., Olsthoorn, L.H.M., Petersen, G.C., Giro, P.E., Kluever, V., Agüi-Gonzalez, P., Grewe, K., Bao, G., Beuermann, S., et al. (2021). Extracellular matrix remodeling through endocytosis and resurfacing of Tenascin-R. Nat. Commun. *12*, 7129. https://doi.org/10.1038/s41467-021-27462-7.

52. Pantazopoulos, H., Katsel, P., Haroutunian, V., Chelini, G., Klengel, T., and Berretta, S. (2021). Molecular signature of extracellular matrix pathology in schizophrenia. Eur. J. Neurosci. *53*, 3960–3987. https://doi.org/10.1111/ejn.15009.

53. Pantazopoulos, H., and Berretta, S. (2016). In sickness and in health: perineuronal nets and synaptic plasticity in psychiatric disorders. Neural Plast. *2016*, 1–23. https://doi.org/10.1155/2016/9847696.

54. Glausier, J.R., and Lewis, D.A. (2013). Dendritic spine pathology in schizophrenia. Neuroscience *251*, 90–107. https://doi.org/10.1016/j.neuroscience.2012.04.044.

55. Konopaske, G.T., Lange, N., Coyle, J.T., and Benes, F.M. (2014). Prefrontal cortical dendritic spine pathology in schizophrenia and bipolar disorder. JAMA Psychiatr. *71*, 1323–1331. https://doi.org/10.1001/jamapsychiatry.2014.1582.

56. Mitlöhner, J., Kaushik, R., Niekisch, H., Blondiaux, A., Gee, C.E., Happel, M.F.K., Gundelfinger, E., Dityatev, A., Frischknecht, R., and Seidenbecher, C. (2020). Dopamine receptor activation modulates the integrity of the perisynaptic extracellular matrix at excitatory synapses. Cells *9*, 260. https://doi.org/10.3390/cells9020260.

57. Schneider, C.A., Rasband, W.S., and Eliceiri, K.W. (2012). NIH Image to ImageJ: 25 years of image analysis. Nat. Methods *9*, 671–675. https://doi.org/10.1038/nmeth.2089.

58. Perez-Riverol, Y., Bai, J., Bandla, C., García-Seisdedos, D., Hewapathirana, S., Kamatchinathan, S., Kundu, D.J., Prakash, A., Frericks-Zipper, A., Eisenacher, M., et al. (2022). The PRIDE database resources in 2022: a hub for mass spectrometry-based proteomics evidences. Nucleic Acids Res. *50*, D543–D552. https://doi.org/10.1093/nar/gkab1038.

59. Evanko, S.P., Chan, C.K., Johnson, P.Y., Frevert, C.W., and Wight, T.N. (2018). The biochemistry and immunohistochemistry of versican. In Methods in Cell Biology, Robert P. Mecham, ed. (Elsevier), pp. 261–279. https://doi.org/10.1016/bs.mcb.2017.08.015.

60. Suresh, A., and Dunaevsky, A. (2016). Preparation of synaptosomes from the motor cortex of motor skill trained mice. Bio Protoc. *5*, e1398.

61. Watzlawik, J.O., Kahoud, R.J., Wootla, B., Painter, M.M., Warrington, A.E., Carey, W.A., and Rodriguez, M. (2016). Antibody binding specificity for

kappa (V_κ) light chain-containing human (IgM) antibodies: polysialic acid (PSA) attached to NCAM as a case study. JoVE, 54139. https://doi.org/10.3791/54139.

62. Sethi, M.K., Downs, M., and Zaia, J. (2020). Serial in-solution digestion protocol for mass spectrometry-based glycomics and proteomics analysis. Mol. Omics *16*, 364–376. https://doi.org/10.1039/D0MO00019A.
63. Mastronarde, D.N. (2005). Automated electron microscope tomography using robust prediction of specimen movements. J. Struct. Biol. *152*, 36–51. https://doi.org/10.1016/j.jsb.2005.07.007.
64. Berretta, S., Pantazopoulos, H., and Lange, N. (2007). Neuron numbers and volume of the amygdala in subjects diagnosed with bipolar disorder or schizophrenia. Biol. Psychiatry *62*, 884–893. https://doi.org/10.1016/j.biopsych.2007.04.023.
65. Peters, A. (2004). A fourth type of neuroglial cell in the adult central nervous system. J. Neurocytol. *33*, 345–357. https://doi.org/10.1023/B:NEUR.0000044195.64009.27.
66. Chidambaram, S.B., Rathipriya, A.G., Bolla, S.R., Bhat, A., Ray, B., Mahalakshmi, A.M., Manivasagam, T., Thenmozhi, A.J., Essa, M.M., Guillemin, G.J., et al. (2019). Dendritic spines: revisiting the physiological role. Prog. Neuro-Psychopharmacol. Biol. Psychiatry *92*, 161–193. https://doi.org/10.1016/j.pnpbp.2019.01.005.
67. Team, R. (2005). A Language and Environment for Statistical Computing (R foundation for Statistical Computing). http://wwwr-projectorg/indexhtml.
68. Tyanova, S., Temu, T., and Cox, J. (2016). The MaxQuant computational platform for mass spectrometry-based shotgun proteomics. Nat. Protoc. *11*, 2301–2319. https://doi.org/10.1038/nprot.2016.136.
69. Tyanova, S., Temu, T., Sinitcyn, P., Carlson, A., Hein, M.Y., Geiger, T., Mann, M., and Cox, J. (2016). The Perseus computational platform for comprehensive analysis of (prote)omics data. Nat. Methods *13*, 731–740. https://doi.org/10.1038/nmeth.3901.

STAR★METHODS

KEY RESOURCES TABLE

REAGENT or RESOURCE	SOURCE	IDENTIFIER
Antibodies		
Anti-CS56	Sigma-Aldrich	C8035; RRDI:AB_476879
Anti-CS56 (for immunoblot and affinity purification)	Abcam	ab11570: RRDI:AB_298176
Anti-Arc/Arg3.1	Proteintech	16290-1-AP; RRDI:AB_2151832
Anti-PSD95	Abcam	ab90426; RRID:AB_2050168
Anti-Versican	Merck	AB1032, RRID:AB_2214376
Anti-Versican (for immunoblot)	Santa Cruz	sc-25831; RRID:AB_2241501
Anti-aggrecan (for immunoblot)	Abcam	ab36861; RRID:AB_722655
Anti-Parvalbumin	Synaptic Systems	195 006; RRID:AB_2619887
Anti-Chondroitin Sulfate A mAb (Clone 2H6)	Cosmo Bio	CAC-NU-07-001
Mouse IgM isotype control	Thermo Fisher	14-4752-82; RRID:AB_470123
Mouse IgM isotype control	Santa Cruz	sc-3881; RRID:AB_737292
Alexa Fluor® 647 Goat anti-mouse	Abcam	ab150115; RRID:AB_2687948
Alexa Fluor® 594 Goat anti-mouse	Abcam	ab150116; RRID:AB_2650601
Alexa Fluor® 405 Goat anti-Rabbit	Abcam	ab175652; RRID:AB_2687498
Alexa Fluor® 647 Goat anti-Rabbit	Abcam	ab150079; RRID:AB_2722623
Alexa Fluor® 488 Donkey anti-goat	Abcam	ab150129; RRID:AB_2687506
Alexa Fluor® 405 Goat anti-Chicken	Abcam	ab175674; RRID:AB_2890171
Alexa Fluor® 546 Goat anti-Mouse	Thermo Fisher	A-11003; RRID:AB_141370
Bacterial and virus strains		
pAAV_U6_VCAN_shRNA_GFP	Dr. Dityatev's group	N/A
pAAV_U6_scramble_shRNA_GFP	Mitlöhner et al.[56]	N/A
Competent *E. coli*	NEB	C3040H
Biological samples		
Human postmortem Amygdala sample from healthy donor	Harvard Brain Tissue Resource Center/NIH NeuroBioBank	N/A
Chemicals, peptides, and recombinant proteins		
Bovine serum albumin (BSA)	Thermo Fisher	BP1605100
Paraformaldehyde (PFA; powder)	Sigma-Aldrich	P6148
Glutaraldehyde	Sigma-Aldrich	G6257
Sodium cacodylate	Sigma-Aldrich	C0250
Hydrogen peroxide	Fisher	H325100
Glycine	Sigma	G-7403
Triton X-100	Fisher	AC215680010
Goat serum	Gibco	16210-064
Streptavidin - Horseradish peroxidase	Invitrogen	434323
3,3'-Diaminobenzidine Tetrahydrochloride	Sigma	D5905-100TAB
Cytoseal	Thermo Fisher	8310-16
Fluomount	Southern biotech	0100-01
Chondroitinase ABC	amsbio	AMS.E1028-10
Halt™ Protease Inhibitor Cocktail	Thermo Fisher	78429
Sodium borohydride	Fisher	AC448501000
Formic Acid/Acetonitrile 0.1/99.9, v/v	Sigma-Aldrich	159002
Ammonium hydroxide	Sigma-Aldrich	221228
Blocking Buffer	Li-Cor	92760001

(*Continued on next page*)

Continued

REAGENT or RESOURCE	SOURCE	IDENTIFIER
NuPage Bis-Tris	Thermo Fisher	NP0335BOX
Mercaptoethanol	Sigma-Aldrich	M3148
Trifluoracetic acid	Sigma-Aldrich	808260
Uranyl acetate	Sigma-Aldrich	M1775
Embed 812 resin	Electron Microscopy Sciences	14900
Fetal Bovine Serum	Life Technologies	10270106
PBS pH 7.4	Life Technologies	10010015
DMEM, high glucose	Life Technologies	41965062
HBSS	Life Technologies	14175053
Iscoves Modified Dulbecco Media	Sigma Aldrich	I3390
Laminin	Sigma Aldrich	L2020
Poly-L-Lysine	Sigma Aldrich	L2636
Trypsin-EDTA (0.05%)	Life Technologies	25300054
Penicillin-Streptomycin (10,000 U/mL)	Life Technologies	15140122
L-Glutamine	Life Technologies	25030024
B27 Supplement	Life Technologies	17504044
Neurobasal Media	Life Technologies	21103049
Critical commercial assays		
Pierce™Silver Stain kit	Thermo Fisher	24612
SimplyBlu™SafeStain	Thermo Fisher	LC6060
Protein L Sepharose	Abcam	ab193261
M-270 Epoxy beads	Thermo Fisher	14301
BCA protein assay	Thermo Fisher	A55860
DNA/RNA Extracol kit	EURX	3750
1X HALT protease inhibitor	Thermo FIsher	P187786
High-Capacity cDNA Reverse Transcription Kit	Applied Biosystems™	4368814
TaqMan gene expression array	Thermo FIsher	4331182
TaqMan™ Fast Universal PCR Master Mix	Applied Biosystems™	4352042
Deposited data		
Mouse proteomic raw data	This Manuscript	PXD047129 https://doi.org/10.6019/PXD047129
Human proteomic data	This Manuscript	PXD050008 https://doi.org/10.6019/PXD050008
Experimental models: Cell lines		
HEK 293T cells	ATCC	CRL-1573
Primary hippocampal culture	This manuscript	N/A
Experimental models: Organisms/strains		
c57bl/6j - Males	The Jackson Laboratory	000664
B6 Cg-Tg(Thy1-YFP)HJrs/J - Males	The Jackson Laboratory	003782
C57BL/6NCrl - Males	Charles River	027
Oligonucleotides		
Gapdh	TaqMan	Mm99999915_g1
Vcan	TaqMan	Mm01283063_m1
Chst3	TaqMan	Mm00489736_m1
Chst7	TaqMan	Mm00491466_m1
Chst11	TaqMan	Mm00517562_m1
Chst12	TaqMan	Mm00546416_s1
Recombinant DNA		
pAAV-U6-GFP Expression Vector	Cell Biolabs	VPK-413

(*Continued on next page*)

Continued

REAGENT or RESOURCE	SOURCE	IDENTIFIER
pAAV_U6_VCANshRNA_GFP	This manuscript	N/A
pAAV_U6_CtrlshRNA_GFP	Mitlöhner et al.[56]	https://doi.org/10.3390/cells9020260
pAAV_U6_scramble_shRNA_GFP	Mitlöhner et al.[56]	https://doi.org/10.3390/cells9020260
Software and algorithms		
ImageJ/FIJI	Schneider et al.[57]	https://imagej.net/software/fiji/
Prism (version 8)	GraphPad	https://www.graphpad.com/scientific-software/prism
PATCHMASTER	HEKA	https://www.heka.com/downloads/downloads_main.html#down_patchmaster
StereoInvestigator 6.0	Micro-Brightfield	N/A
Leica LAS-X software	Leica	N/A
Other		
Vibratome	Leica	VT1200S
Microtome	American Optical	860
Cryostat	Leica	CM1950
Double edge, breakable style razor blades	Cetim	AISI 440
Low-profile disposable cryostat blades	Leica	DB80LX
Automatic tissue homogenizer	Avantor	SCERSP749540-0000
Disposable pestles, PP, 1.5mL	Avantor	SCERSP749521-1500
5600+ QTOF mass spectrometer	Sciex	N/A
Q-Exactive HF mass spectrometer	Thermo Fisher	N/A
nanoAcquity UPLC	Waters	N/A
Eksigent nanoLC.as-2 autosampler	SpectraLab	Others-00-001
NANOSpray® III Source	Sciex	p/n 1034661
Acclaim PepMap100	Thermo Fisher	164946
IntegraFrit Trap Column	New Objective	N/A
Odyssey Scanner	Li-Cor	N/A
Bio-Rad semidry transblotters	Bio-Rad	N/A
Standard surgical blades	Word Precision Instruments	500240
SuperFrost Ultra Plus™ Gold slides	Fisher scientific	11976299
Pierce™ C18 Spin tips and columns	Thermo Fisher	87782
EPC-10 amplifier	HEKA Elektronik	N/A
Quant-Studio-5 device	Applied Biosystems	A28569
Zeiss Axio Imager M2 fluorescent microscope	Zeiss	M2: 430004-9902
Stereotactic frame	Narishige Scientific Instrument Lab	SR-6M
Ultra microinfusion pump	World Precision Instrument	UMP3
Confocal laser scanning microscope	Leica	TCS SP8
Scanning electron microscope JEM 1200EX II	JEOL	N/A
Zeiss Axioskop 2 Plus	Zeiss	SM100297-MG1
6 well cell culture plate	Greiner Bio One	GB657160

RESOURCE AVAILABILITY

Lead contact

Further information and requests for resources should be directed to and will be fulfilled by the lead contact, Sabina Berretta (s.berretta@mclean.harvard.edu).

Materials availability

- The AAV vector carrying versican shRNA was generated for this work. It has not been deposited in a public repository but will be freely available upon request.

Data and code availability

- The mouse mass spectrometry proteomics data have been deposited to the ProteomeXchange Consortium via the proteomics identification database (PRIDE)[58] partner repository with the dataset identifier PXD047129. Project accession: PXD047129. These data are also available as part of the supplemental material. The human mass spectrometry proteomics data have been deposited to the ProteomeXchange Consortium via the PRIDE partner repository with the dataset identifier PXD050008. Project accession: PXD050008.
- This paper does not report original code.
- Any additional information required to reanalyze the data reported in this work paper is available from the lead contact upon request.

METHOD DETAILS

Animals

All experimental mice were group housed (3–5 mice per cage) on a 12:12hr light-dark cycle in a temperature-controlled colony room and had unrestricted access to food and water. All experiments were performed in young adult male mice (90-180 days old; weight 23-28 g).

All procedures were conducted in accordance with policy guidelines set by the National Institutes of Health and were approved by the McLean Institutional Animal Care and Use Committee, the Animal Welfare Committee of the University of Trento, and the Italian Ministry of Health and by the Ethical Committee on Animal Health and Care of the State of Saxony-Anhalt (TVA 2502-2-1343) according to animal research ethics standards defined by German law.

Sensory deprivation, electron microscopy, mouse proteomics and ARC studies

C57BL/6 wild-type male mice were purchased from The Jackson Laboratory. Mice were let to habituate to the housing conditions in the McLean Hospital animal facility for a week before being used for experiments.

Sensory stimulation study

C57BL/6 mice were originally purchased from Charles River and bred in the animal facility of the University of Trento.

Dendritic spine analysis

Thy1-eYFP mice were originally purchased by The Jackson laboratory and bred in the McLean Animal facility.

Versican-shRNA experiments

C57BL/6 mice were bred in the core animal facility of DZNE (Magdeburg) and transferred to a small vivarium and housed in individual cages for at least 72 hours before the experiments. Behavioral experiments were conducted during the dark phase of the cycle.

Human postmortem specimen

Fresh-frozen human postmortem amygdala tissue samples from one healthy donor were obtained from the Harvard Brain Tissue Resource Center (HBTRC; McLean Hospital, Belmont MA).

The HBTRC, one of the National Institute of Health NeuroBioBank repositories, operates under an Institutional Review Board (IRB; Massachusetts General Brigham) protocol covering all its procedures, including informed consent process, collection of tissue and donors' data and distribution to investigators within the USA and across the world. Tissue and donors' data distributed to investigators is de-identified. Several regions from each brain were examined by a neuropathologist. The subject used for this study did not present with evidence for gross and/or macroscopic brain changes, or clinical history, consistent with cerebrovascular accident or other neurological disorders. Frozen tissue blocks containing the amygdala were placed in a cryostat maintaining a constant temperature between -13° and -15 °C. The borders of the amygdala were lightly 'etched' using a surgical blade (Word Precision Instruments, 50040) so that collected sections did not contain surrounding brain regions. Tissue sections were collected onto superfrost slides (Fisher scientific, 11976299).

Cell lines

HEK 293 cell line was purchased from ATCC (CRL-1573). Cells were grown in Iscoves Modified Dulbecco media (Sigma Aldrich, I3390) with 10% FBS (Life Technologies, 10270106) and 1% L-Glutamine (Life Technologies, 25030024). The cells were maintained at 37 °C in a humidified incubator with 5% CO_2. Cells were subcultured every three days.

Primary cell culture

Hippocampal cells were isolated from embryonic (E18) C57BL6/J mice. Briefly, the pups from pregnant mice were carefully removed and brains were put in a Petri dish filled with 50 mL ice-cold HBSS (Life Technologies, 14175053). The hippocampi were isolated and collected in 15 mL conical tube, filled with cold PBS (Life Technologies, 10010015), followed by transferring the hippocampi to 2 mL of 0.05% Trypsin/EDTA (Life Technologies, 25300054) and incubated for 15 min in 37 °C. To stop the digestion, Trypsin was removed and 1 mL of cold DMEM (Life Technologies, 41965062) supplemented with 10% FBS (Life Technologies, 10270106), 1% L-Glutamine (Life Technologies, 25030024) and 1% Penicillin/Streptomycin (Life Technologies, 15140122) was added to the hippocampi. Tissue

dissociation was completed by pipetting up and down followed by cell counting and seeding with a density of 5 × 10^5 cells per well in a 6-well plate (Greiner Bio One, 657160) in 2.5 mL DMEM medium supplemented with 2% B27 supplement (Life Technologies, 17504044), 1% L-glutamine (Life Technologies, 25030024), and 1% Pen-Strep (Life Technologies, 15140122). The 6-well plates were precoated with 7:3 mixture of 100μg/mL PLL (Sigma Aldrich, P2636) and 25μg/mL Laminin (Sigma-Aldrich, L2020) for 1 ½ hours in incubator at 37°C, followed by washing the wells with sterile ddH2O. After 4 hours, medium was exchanged to 2.5 mL of Neurobasal+ medium (Life Technologies, 21103049) supplemented by 2% B27 supplement, 1% L-glutamine, and 1% Pen-Strep. Cells were maintained at 37°C in a humidified 5% CO_2 incubator. On DIV 7, cells were transduced with AAVs and mRNA expression levels were assayed at DIV 21.

Tissue preparation

For electron microscopy study

Mice were deeply anesthetized with isoflurane and perfused transcardially with 50 mL phosphate buffer/saline (PBS) followed by 50 mL PFA-glutaraldehyde-NaCacodylate (4% PFA, 0.1% glutaraldehyde, 0.1M Sodium Cacodylate, 0.21 mg/mL $CaCl_2$, 0.1M Sucrose). Brains were postfixed in PFA-NaCacodylate (4% PFA, 0.1M Na Cacodylate, 0.21mg/mL $CaCl_2$, 0.1M Sucrose) for 2 hours. Fixed brains were kept overnight at 4°C in phosphate buffer saline (PBS) and sectioned on a vibratome (Leica VT1200S) at 40 μm thickness. Sections for each animal were collected in PBS and processed 24 hours later for immunohistochemistry.

For light and fluorescent microscopy studies

Mice were deeply anesthetized with isoflurane (urethane for sensory stimulation experiment, see below) and perfused intracardially with a 50 mL 0.1M phosphate buffer (PB), followed by 50 ml of 4% PFA; pH 7.4. Brains were harvested and post-fixed overnight in 4% PFA, then switched to a cryoprotectant solution (80% PB, 20% glycerol with 0.1% sodium azide). Cryoprotected brains were sectioned on a freezing sliding microtome (American Optical 860, Buffalo, NY, USA), and serial sections (30 μm thickness) were collected in 24 separate compartments to be stored at 4°C in cryoprotectant solution.

Immunostainings

Pre-embedding immunolabeling for electron microscopy

All solutions were made in 0.1 PBS and all steps were preceded and followed by washes consisting of 3 consecutive 5 min rinses in PBS, unless otherwise specified. Free-floating tissue sections were rinsed in PB, treated with 0.3% Hydrogen peroxide (Fisher, H325100) for 15 min, and incubated in a solution of 0.05% sodium borohydride (Fisher, AC448501000), 0.1% Glycine (Sigma, G-7403) for 30 min. Next, the sections were incubated in blocking solution (4% Bovine serum albumin (Fisher, BP1605100), 10% Goat serum (Gibco, 16210-064), 0.01% Triton X-100 (Fisher, AC215680010)) for 90 min, then transferred in primary antibody solution (1:1000 CS56, 2% BSA, 2% Goat serum, 0.01% Triton X-100) for 2 days. A subset of sections was incubated without a primary antibody as a negative control. The sections were then incubated in biotinylated anti-mouse IgM secondary antibody (Vector labs, BA-2020) 1 to 500 μL) for 2 h, followed by incubation in Streptavidin-HRP (Invitrogen, 434323) (1:5000) for another 2 h. Finally, tissue sections were washed with PB and incubated with 3,3'-Diaminobenzidine Tetrahydrochloride (Sigma, D5905-100TAB) 0.5 mg/mL in 0.1 M Sodium Cacodylate, 0.005% hydrogen peroxide for 20 min. The reaction was stopped and sections were washed with PB and processed for EM (see below).

For light microscopy

All solutions were made in 0.1 PBS containing 0.2% Triton X-100 (Fisher, AC215680010) (PBS-Tx) and all steps were preceded and followed by washes consisting of 3 consecutive 5 min rinses in PBS-Tx unless otherwise specified.

Step 1. Free-floating tissue sections were washed for 90 min, then pre-treated overnight with antigen retrieval solution at 37°C (1.8mM DTT, 1.8mM EDTA, 12mM Citric Acid, 43mM, 43mM Na_2HPO_4, 0,05% bovine serum albumin (BSA) in deionized-distilled H_2O). Sections were then incubated in 0.03 % H_2O_2 solution for 30 min, followed by incubation in blocking solution (2% BSA (fraction V)) for 90 min. Tissue was then transferred to primary antibody solution (2% BSA solution with: see primary antibody concentrations below) and incubated at 4°C for ∼60 h.

Step 2. Sections were incubated with a biotinylated secondary antibody (1:500) for 2 h, followed by streptavidin conjugated with horseradish peroxidase (Zymed, San Francisco, CA, USA. 1:5000) for 2 h. Sections were then rinsed in 0.1M phosphate buffer (PB. 0.1 M sodium phosphate dibasic; 0.1 M sodium phosphate monobasic. Ph: 7.2) and incubated with nickel-enhanced diaminobenzidine/peroxidase (0.02% diamino-benzidine (Sigma, D5905-100TAB), 0.08% nickel-sulfate, 0.007% H_2O_2 in PB). The colorimetric reaction was visually monitored and stopped by washes in PB. Tissue sections were mounted on gelatin-coated slides, dried overnight, dehydrated through serial ethanol-xylene steps, and coverslipped with an xylene-based mounting media (Thermofisher Cytoseal, 8310-16).

For fluorescent microscopy

Step 1. As described above.

Step 2. Tissue sections previously incubated in the primary antibody solution were rinsed, then placed in a fluorophore-conjugated secondary antibody solution for 4 h. Sections were then washed 5 min in PB, mounted on gelatin-coated slides, dried for 1 h, and coverslipped with fluorescent mounting medium (Southern biotech 0100-01).

Triple labeling immunofluorescence for CS56-PV-Versican

The brain samples were preserved using 4% PFA in PBS overnight and then immersed in 30% sucrose in PBS for 48 hours. Afterward, the brains were frozen in 100% 2-methyl butane at -80°C and cut into coronal sections. The sections were washed three times with PB and then permeabilized (0.4 % Triton-X 100 in PB) for 10 minutes at RT, then incubated for 1 hour at RT in blocking solution (10% normal goat serum in PB, 0.4 % glycine, 0.4 % Triton-X100). Primary antibodies were added to the sections for overnight incubation at 37°C with gentle shaking. The next day, slices were washed 3 times with PB for 10 minutes and then incubated with secondary antibodies at RT for 3 hours. Slices were washed 3 × 10 min at RT with PB, then mounted on Superfrost slides and coverslipped using Fluoromount medium (Sigma, F4680).

CS56-versican colocalization immunofluorescence

An optimized protocol was used to ensure the simultaneous detection of CS56 and versican following ChABC. First, slices were stained for CS56 as described above. Thereafter, to cross-link CS56 antibodies and prevent loss of staining following ChABC treatment, slices were fixed overnight in 1% PFA. Subsequently, to remove glycosaminoglycan chains, slides were incubated at 37°C in a humidified chamber with 0.1 Unit/ml ChABC (amsbio, AMS. E1028-10) in a solution comprising 18 mM Tris, 1 mM sodium acetate (pH 8.0) for a period of 2 hours[59]. Following the ChABC treatment, the slices were stained for versican as described above and mounted.

Primary antibodies

CS56. Is a mouse monoclonal IgM (Sigma-Aldrich, C8035) made using vertebral membranes from chicken gizzard fibroblasts as an immunogen,[24] previously shown to detect a subclass of 6-sulfated CSPGs as well as CS-clusters in human and mouse tissue.[22,25–27] The antibody was diluted 1:6000 for light microscopy and 1:3000 for immunofluorescence. 1:200 dilution was used for triple-label experiments.

Anti-Arc/Arg3.1 is an affinity-purified rabbit polyclonal IgG (Proteintech, 16290-1-AP, dilution 1:1000).

Anti-PSD95 is a polyclonal IgG made in goat (Abcam, AB90426, dilution 1:500).

Anti-Versican is affinity chromatography-purified antibody made in rabbit against a.a. 535-598 (GAG alpha Domain) of mouse versican (AB1032, Merck, dilution 1:100).

Anti-Parvalbumin is a polyclonal IgG made in chicken (195006, Synaptic Systems, dilution 1:500).

Anti-Chondroitin Sulfate A is a mouse monoclonal antibody against chondroitin sulfate A ([GlcA-GalNAc(4S)] (CAC-NU-07-001, Cosmo Bio, dilution 1:100).

Secondary fluorophore-conjugated antibodies

Against their respective primary antibodies, Alexa Fluor® 647 Goat anti-mouse, Alexa Fluor® 594 Goat anti-mouse, Alexa Fluor® 405 Goat anti-Rabbit, Alexa Fluor® 647 Goat anti-Rabbit, and Alexa Fluor® 488 Donkey anti-goat was used at a dilution of 1:500. Alexa Fluor® 405 Goat anti-Chicken and Alexa Fluor® 546 Goat anti-Mouse were used with a dilution of 1:1000.

Mass spectrometry (MS) on subcellular fractions from the mouse primary sensory cortex

Cell fractioning

Sixteen young adult mice were briefly anesthetized with isoflurane and sacrificed by decapitation. Brains were excised and the primary somatosensory cortex was freshly dissected according to anatomical landmarks found in the Allen Brain Atlas (https://mouse.brain-map.org/static/atlas). The fractioning protocol was re-adapted from Wirths 2017[38] and Suresh & Dunaevsky 2015[60]. The tissue was mechanically homogenized, using an automatic tissue homogenizer and disposable pestles (Avantor), in 300 μL ice-cold homogenization buffer (320 mM sucrose, 1 mM EDTA (pH8.0), 5 mM Tris Base in ddH_2O). Homogenate was centrifuged at 1,000 xg for 10 minutes at 4°C. The supernatant was saved as fraction S1a. The resulting pellet was resuspended in 300 μL buffer and centrifuged again at 1,000xg for 10 minutes at 4°C. The supernatant (S1b) was once again saved and combined with S1a constituting the fraction S1. The resulting pellet (containing myelin and debris) was discarded. Finally, fraction S1 was centrifuged at 13,000xg for 20 minutes at 4°C. The supernatant (S2), containing light membranes and enzymes was saved for proteomics. The pellet (P2), containing microsomal preparation enriched in synaptosomes was washed in 500 μL homogenization buffer by spinning it again at 13,000xg for 20 minutes at 4°C. The supernatant resulting from this last wash was discarded while the washed pellet was resuspended in ice-cold immunoprecipitation lysis buffer (0.5 M NaCl, 0.5 mM EDTA, 1% Triton-X-100, 50 mM Tris pH 7.5 in ddH_2O) containing 1X HALT protease inhibitor (Thermo Fisher P187786). The protein concentration for both S2 and P2 was assessed using a Bio-Rad protein assay kit, according to manufacturer instructions, before being used for proteomics.

Immunoprecipitation

IP protocol was adapted from Watzlawik et al. 2016[61]. Manufacturer's guidelines were followed for the use of protein L/Sepharose beads (Protein L Sepharos. Abcam, ab193261). To obtain enough proteins to run a proteomic study after immunoprecipitation, both S2 and P2 samples were combined into pools. Each pool contained lysates derived from four different animals, thus obtaining 4 pools for the S2 preparation and 4 pools for the P2.

Preparation of L/Sepharose beads. 200ul of IP buffer (0.15 M NaCl, 0.5 mM EDTA, 1% Triton X-100, 0.05% SDS, 50 mM Tris buffer, pH 7.5, 1x HALT protease inhibitor cocktail) were added to 15 μL of protein L/Sepharose slurry and gently mixed. The mixture was centrifuged for 2 minutes at 1,000xg at 25°C. The supernatant was discarded. This process was repeated 3 times, and then 200 μL of IP buffer was added to the pellet and left overnight at 4°C while gently shaking.

Antibody-antigen complex formation. 1 μL of CS56 antibody (Sigma C8035), or 1 μL of IgM control Isotype (clone 11E10, Invitrogen 14-4752-82) were added to 350 μg of protein lysate (for each sample) and let gently shaking overnight at 4°C.

Antibody-Antigen-L/Sepharose L Complex formation. L/Sepharose beads were centrifuged for 2 minutes at 1,000 xg, 4°C, supernatant was discarded. The antibody-antigen complex solution was added to the washed beads and incubated for 2 hours while rocking at 4°C. The resulting suspension was centrifuged for 2 minutes at 1,000xg at 4°C, supernatant was removed. The pellet was washed twice by adding 1ml of ice-cold IP buffer containing 0.2% BSA and spinning for 2 minutes at 1,000xg, 4°C. A third wash was finally performed adding 1ml ice-cold IP buffer to the pellet and spinning down the suspension for 2 minutes at 1,000xg, 4°C. The supernatant was discarded.

Elution. For each sample, 30 μL of IP elution buffer *(59 μL IP buffer, 31ul 4xconc NuPage LDS, 10 μL DTT*) was added to the pellet containing Antibody-Antigen-L/Sepharose complex. Samples were first heated at 95°C for 5 minutes, then moved into ice for 2 minutes and finally centrifuged for 30 sec at 13,000 xg, 4°C.

Gel run. 10 μL of each eluted sample was run on SDS-polyacrylamide gel for 75 minutes at 150V. After the run, the gels were stained using SimplyBlu™SafeStain (Biorad, Thermo Fisher LC6060) to visualize protein bands. The CS56-specific band (~80kDa) was excised and used for proteomics. A secondary identical gel was run in parallel and colored using the Pierce™Silver Stain kit (Thermo Fisher, 24612) according to the manufacturer's instructions, to obtain a better-quality image for publication (as shown in Figure 4C).

In-gel trypsin digestion and peptide de-salting

The appropriate gel bands from S2 and P2 were excised using a scalpel on a glass plate. Each gel band was shredded into smaller pieces and placed in Eppendorf tubes containing 200 μL of 50 mM ammonium bicarbonate. The gel bands were destained from Coomassie bright-blue using 200 μL of de-staining solution (50% acetonitrile and 50% 50 mM ammonium bicarbonate) and incubated on a thermomixer for 30 min. This step was repeated 1-2 times until the gel pieces showed the absence of a blue stain. A 100 μL quantity of 10 mM dithiothreitol was added and samples were incubated at 60°C for 30 min. The dithiothreitol was removed and 100 μL acetonitrile was added, and the solution was incubated on a thermomixer for 5 min at RT. Acetonitrile was removed from the gel fragments, 50 mM iodoacetamide was added, the solution was incubated in the dark at RT for 1 h, and then gel fragments were washed with three rinse cycles of 100 μL acetonitrile followed by 100 μL water for 5 min each, followed by one rinse cycle of 100 μL 1:1 acetonitrile:water for 5 min. The solution was removed, and gel pieces were dried using a centrifugal vacuum evaporator for approximately 30 min. After drying, a 0.1 μg quantity of trypsin (Promega) (0.1 μg/μL, 10 μL) enzyme was added to each sample, and allowed to absorb on the gel pieces on ice for 5-10 min. Next, a 100 μL volume of 50 mM ammonium bicarbonate was added to each sample to cover gel pieces and the samples were digested overnight at 37°C. The digested peptides were then collected into a new Eppendorf tube, and the gel pieces were washed with 100 μL of 80% acetonitrile/20% water/0.1 % trifluoracetic acid (TFA) on thermomixer for 10 min. The solution was combined with the first peptide solution, and dried in a centrifugal vacuum evaporator. Dried peptides were resuspended in 10 μL of 2% acetonitrile/ 98% water/ 0.1 % TFA solution and cleaned using Thermo/Pierce C18 ZipTips (10 μL bed volume). The C18 ZipTips were washed once with 10 μL of 50:50 acetonitrile: water and then three times using 10 μL of 2% acetonitrile/ 98% water/ 0.1 % TFA solution. The resuspended peptides were pipetted onto a C18 ZipTip and then washed three times with 10 μl of 2% acetonitrile/ 98% water/ 0.1 % TFA. Cleaned peptides were eluted using three 10 μL volumes of 60% acetonitrile/ 40% water/0.1% TFA solution. The eluted peptides were dried in a centrifugal vacuum evaporator and stored at -80°C until LC-MS/MS analysis.

Liquid chromatography-tandem mass spectrometry (LC-MS/MS) analysis

Nano-LC-MS/MS separation was performed using a nanoAcquity UPLC (Waters Technology) and Q-Exactive HF mass spectrometer (Thermo-Fisher Scientific) according to Sethi et al[62]. Reversed phased C-18 analytical (BEH C18, 150 μm x 100 mm) and trapping (180 μm x 20 mm) columns from Waters technology were used. Trapping was performed at 4 μL/min flow for 4 min with 100% A, and a 75 min method was used with a gradient from 2 to 98% acetonitrile in 97 min, using 99% water / 1% acetonitrile/ 0.1% formic acid as mobile phase A and 99% acetonitrile/ 1% water /0.1% formic acid as mobile phase B at a flow rate of 0.5 μL/min. Data-dependent acquisition tandem MS was acquired in the positive ionization mode for the top 20 most abundant precursor ions. Spray voltage for positive mode was zero. The capillary temperature and probe heater temperature were kept at 250 and 350, respectively, and max spray current and S-lens RF level both were kept at 50. For MS global settings, chromatographic peak width (FWHM) of 15 s, and customized tolerance and dynamic exclusion of 10 ppm were used. Full MS scans were acquired from *m/z* 350–2000 with 60,000 resolutions using an automatic gain control (AGC) target of $3e^6$ and a maximum IT of 100 ms. Dynamic exclusion (12 s) was enabled. The minimum AGC target was set at $5e^3$, and the intensity threshold was set at $1e^5$. Precursor ions were fragmented using 2 microscans at a resolution of 15,000 with a maximum injection time of 50 ms and an AGC target of $2e^5$ using higher energy collision-induced dissociation (HCD) with stepped normalized collision energy of 27, 35 V. The complete LC-MS/MS instrumental settings are given in the raw data files deposited to the PRIDE[58] repository dataset identifier PXD047129 and https://doi.org/10.6019/PXD047129.

Microscopy

Electron microscopy

Immunostained tissue sections were postfixed in 1% OsO4, dehydrated in graded ethanol series and extra-dry acetone, and flat embedded in Embed 812 resin. Ultrathin sections (~80 nm) were collected on Formvar-coated slot grids. A set of sections was left unstained and a second set was post-stained with uranyl acetate (saturated solution) and Reynold's lead citrate, before being analyzed. Sections were imaged on a JEOL JEM-1200 EX II with a 1k CCD camera, and on a Tecnai F20 (200 keV) transmission

electron microscope (FEI, Hillsboro, OR); the images were collected using a 2 K × 2 K charged-coupled device (CCD) camera, at 19,000X magnification (1.12 nm pixel size). Whole CSC photocomposites were acquired as automated montages of overlapping high-magnification images using the microscope control software SerialEM [63].

Stereology-based quantitative microscopy

Zeiss Axioskop 2 Plus interfaced with StereoInvestigator 6.0 (Micro-Brightfield, Williston, VT, USA) was used for quantifications. Anatomical landmarks, including subdivisions into cortical layers, were identified according to Allen Brain Atlas (https://mouse.brain-map.org/static/atlas). Serial sections, sampling the full rostro-caudal extent of the regions of interest (each sampling interval was of 720 μm: meaning the number of serial sections between each quantified slice, or cutting interval = 24 multiplied for 30 μm thickness of each slice), were taken into account, thus respecting the equal opportunity rule. Estimation of numerical densities was carried out as follow[64]:

The volume (V) of the brain areas was estimated according to the formula: $V = \Sigma a * z * i$.

Where Σa is the surface area of each region of interest, obtained by delineating the borders of the area using the StereoInvestigator 6.0 software tracing tool; z is the section thickness (30 μm); and i is the cutting interval (24) between sections.

The numerical estimates (NE) were calculated using the formula: $NE = \Sigma_{CSCs} * i$.

Were Σ_{CSCs} is the total number of CSCs counted across the multiple sampled sections, and i is the cutting interval (24).

Numerical densities (NDs) were then calculated as: $NDs = NE / V$.

The contralateral bias index was calculated using the formula: CBI=NDs Right hemisphere/(NDs Right hemisphere + NDs left hemisphere).

Quantification of CSCs in layer 1 was not taken into account due to recurrent inconsistent results, likely a consequence of CS56 antibody accumulation into the pial surface (also see Figure S2).

Multiple fluorescent microscopy

A Zeiss Axio Imager M2 with a Lumencor SOLA LED lamp interfaced with StereoInvestigator 10.0 (Microbrightfield Inc., Williston, VT) was used for elements quantification in the neural tissue.

Confocal microscopy

A confocal laser scanning microscope Leica TCS SP8, equipped with an HC PL APO 100x/1.40 oil objective interfaced with Leica LAS-X software was used. Images were recorded at high resolution (1024 pixels square), 400 Hz scan speed, in sequential imaging mode. Excitation/emission wavelengths used were: 490/520 for Alexa 488 fluorophore and 640/670 for Cy5 647 fluorophore. For Vcan/CS56/PV triple labeling experiment a confocal Zeiss LSM 700 microscope was used. Z-stack images of hippocampal CA1 were obtained with the 40× objective at 0.5× digital zoom. The acquisition conditions were maintained throughout all imaging sessions.

Details for elements quantification in microscopy experiments

CSCs classification

CSCs present with distinct morphological characteristics, such as a round shape with a diameter of 70-100 μm (in rodents) often enveloping several unstained cell bodies (examples in Figures S1A–S1C). CSC morphological features, such as sharply labeled processes and diffuse punctate labeling, are present to different degrees across a spectrum. For practical quantification purposes, we assigned CSCs to two discrete categories, i.e. R-CSC and D-CSC, depending on their predominant morphological features. CSCs with negligible punctate labeling and predominant sharply labeled converging processes were classified as R-CSC (Figures 1F and S1A). CSCs with a predominant pattern of diffuse immunolabeled puncta, lacking distinctive signs of immunolabeled processes, were categorized as D-CSC (Figures 1G and S1B). CSCs presenting both sharply defined processes and dense punctate labeling simultaneously were classified as an intermediate category (Figure S1C). This latter category is speculated to be a transitioning phase between the two ends of the morphological spectrum. According to our EM data, punctate labeling within CSCs corresponds to peri-synaptic labeling. Thus, it is reasonable to conclude that both D-CSCs and intermediate clusters present dense peri-synaptic accumulation of CS56 and they are both subsequent steps with respect to R-CSCs. For this reason, intermediate types were included in the D-CSC group for quantification purposes. This strategy allowed to reduce the number of forced choices to make during subjective classification in the quantitative microscopy experiments, limiting the amount of mislabeling in the data while preserving the conceptual outcome of the study.

For all studies where CSC numerical densities estimation was not required (co-localization with PSD95, electron microscopy, dendritic spine analysis and CSCs-ARC co-localization), only prototypical R-CSCs and D-CSCs were used.

Electron microscopy analysis

One prototypical R-CSC and one D-CSC were acquired from an adult (P80) wild-type mouse and compared. High magnification (19,000x) montages of whole CSCs in not-counterstained sections were deconstructed in multiple quadrants (8.6x4.5 μm) and inspected using StereoInvestigator 6.0 software. Inside each field, CS56 immunoreaction products were manually quantified. Glial processes were recognized according to Peters[65] (Figures S3 and 4). Each independent immunoreaction product within a glial cell process was quantified as a single element (Figures 1F, 1G, S3, and S4). When positive immunoreaction was observed within the edge of a glial cell process adjacent to a pre-or-post synaptic compartment the element was categorized as "glia endfoot" (Figure S3. Blue

stars). Synapses, identified by their distinct pre- and post-synaptic elements, were counted as positive (CS56-coated) when showing clearly distinguishable black immunoreaction product within the synaptic cleft and/or coating the pre- and post-synaptic elements (Figures 2 and S4).

CS56-PSD95 co-localization analyses

Z-stack (0.5μm optical thickness) images within D-CSC and size-matched areas outside CSC were acquired from the BCx, at 100x magnification. The choice of quantifying D-CSC was based on the fact that prominent glial processes immunolabeling within R-CSC rendered synaptic quantification unreliable. Individual stacks were quantified using StereoInvestigator 6.0 software, using a standardized counting strategy. Partially overlapping puncta labeling, with less than 1-pixel distance between the PSD95- and CS56-IR puncta, were classified as juxtaposed.

CSCs co-localization with ARC$^+$ dendrites

8 slices from 4 animals, double stained for both ARC and CS56, were investigated using a Zeiss Axio Imager M2 fluorescent microscope with a Lumencor SOLA LED lamp interfaced with StereoInvestigator 10.0 (Microbrightfield Inc., Williston, VT). First, ARC-positive dendrites were identified in the BCx, and marked. Second CSCs were identified and classified into their morphological categories (R-CSCs and D-CSCs) in the same region and annotated. Finally, the two channels were merged and we quantified the number of annotated ARC-positive dendrites overlapping with the 3-dimensional extension of CSCs.

Dendritic spines morphometric analysis

Z-stack (0.5μm optical thickness) images of YFP-labeled dendrites were acquired in layers II/III at 100x magnification. For each dendrite, two sets of images were collected, one of a stretch located within a CSC and a second of a stretch of the same dendrite located outside the CSC (control condition). Dendritic spines were classified into five different categories according to their morphological features: mushroom, stubby, thin, filopodia, and cups[66]. Only a marginal fraction of cups and filopodia were observed, thus they were not included in this analysis. Dendritic spine density was defined as the number of dendritic spines/length of dendritic stretch (in μm).

Head length, head width, and neck length of each mushroom spine were measured using the measuring tool item included in the Leica LAS-X software (see also Figure S6). *Neck length* was defined by the length from the most medial point of the base of the neck to the most medial point of the most distal aspect of the neck. *Head length*, similarly, was measured from the most medial and proximal aspect of the head to the most medial and distal aspect. The *width of the head* was measured at the widest aspect of the head. Total spine length was obtained by combining neck and head length.

Analysis of CS56-reactive CSPGs and versican co-localization using triple fluorescent immunolabeling

To measure the intensity of versican and CS56-immunoreactivity using ImageJ 1.54 software (NIH, USA)[57] we outlined the region of interest (ROI; Barrel cortex or hippocampal CA1) using the tracing tool included in the software. For each sample, the mean fluorescent intensity for both versican and CS56 immunoreactivity was normalized using the MFI derived from the pyramidal neurons labeled using AAV U6-GFP. As an additional test, we used triple fluorescent immunolabeling to run a similar analysis, using parvalbumin cell staining as a normalizing reference signal. To do so, the somata of PV+ cells were outlined manually, enlarged by 0.1 μm, and a band of 0.6 μm and MFI were obtained using ImageJ.

Behavioral paradigms

Whisker trimming

Mice were assigned to a control group (n=6) and a sensory-deprived group (n=5). Sensory deprivation was achieved by closely trimming the right facial vibrissae for 7 consecutive days every 24 hours, under brief isoflurane anesthesia. Control mice were briefly anesthetized daily to uniform experimental conditions. Animals were sacrificed by transcardial perfusion on day 8.

Whisker stimulation

Unilateral whisker stimulation was performed as according to Balasco et al. 2022[35]; the ipsilateral hemisphere served as a control. All mice were anesthetized by intraperitoneal injection of a 20% solution of urethane in sterile double distilled water (1.6 g/kg body weight), placed on a 37°C warming pad, and head-fixed on a stereotaxic frame. Urethane anesthesia was chosen as it preserves whisker-dependent activity in the somatosensory cortex [35]. Mice were kept under anesthesia for 4 hours prior to whisker stimulation. Immediately before whisker stimulation, a subcutaneous saline injection (100-200 μl) was administered to maintain hydration. Additional anesthetics at 10% of the initial dose were administered as needed. Whisker stimulation was performed in three consecutive 5-minute sessions spaced by 1-minute intervals. Each session consisted of unilateral continuous mechanic deflection of the left whiskers using a wooden stick. Mice were kept under constant anesthesia and sacrificed at two different time points, 1h (n=6) and 2h (n=6), following the end of whisker stimulation.

Open field

The open field test involved placing the animals in a 50 x 50 x 30 cm arena and allowing them to move around freely for 10 minutes while being recorded.

Novel object location test (NOLT)

During the encoding phase of the NOLT, the animals were presented with a pair of identical items and allowed to explore for 10 minutes, while during the retrieval phase, one of the items was placed in a novel location. The animals' behavior was assessed based on the time spent investigating the items in familiar (F) and novel locations (N), as well as the discriminating ratio [(N-F)/(N+F)] x 100%. Two control mice with outlaying negative ratios (double Grubbs test, $p<0.0001$) were excluded from behavioral analyses.

Novel object recognition test (NORT)

The NORT was conducted 24 hours after the NOLT retrieval phase and consisted of presenting the animals with a pair of identical items during the encoding phase. One of the items was replaced with a novel object in the retrieval phase. The animals' recognition memory was assessed using the same method as in the NOLT. Both the encoding and retrieval phases of the NORT lasted 10 minutes.

Viral injection for versican knockdown

AAV generation and validation

We utilized a short hairpin RNA (shRNA) strategy to knock down the expression of mouse versican. To create the shRNA plasmid, a target sequence from MISSION predesigned siRNA against mouse versican (Sigma, SASI_Mm02_00296627) was inserted into the AAV U6-GFP backbone (Cell Biolabs Inc) using BamH1 and EcoR1 (New England Biolabs) restriction site. For a non-targeting control, the shRNA universal negative control (Ctrl) from Sigma was used. To generate the AAV, HEK 293 cells were transfected with an equimolar mixture of the shRNA-encoding AAV U6-GFP, pHelper, and RapCap DJ plasmids (Cell Biolabs Inc) using PEI at 1 ng/μL. Following 48-72 hours of transfection, freeze-thaw cycles were used to lyse cells, and then benzonase was added at 50 units/ml and incubated at 37 °C for 1 hour. The lysates were centrifuged at 8000× g at 4 °C, supernatants were collected and filtered through a 0.2-micron filter. The filtrates were purified using pre-equilibrated HiTrap Heparin HP affinity columns (GE HealthCare), followed by washing with wash buffer 1 (20 mM Tris, 100 mM NaCl, pH 8.0) and wash buffer 2 (20 mM Tris, 250 mM NaCl, pH 8.0). Elution buffer (20 mM Tris, 500 mM NaCl, pH 8.0) was then used to elute viral particles, which were further purified using Amicon Ultra-4 centrifugal filters (100 kDa molecular weight cutoff, Merck Millipore) and 0.22 μM Nalgene® syringe filter units (Sigma-Aldrich, Z741696-100EA). Finally, the purified viral particles were aliquoted and stored at -80 °C. To validate the efficiency of the knockdown shRNA, the primary hippocampal neuron was infected at 7 days *in vitro* (DIV) and fed regularly. Cells were then collected at DIV 21 and total RNA was isolated using DNA/RNA Extracol kit (EURX Cat. No. E3750) according to the manufacturer's recommended protocol. The purified RNA was converted to cDNA by using a High-Capacity cDNA Reverse Transcription Kit (Applied Biosystems™, Cat.4368814). Gene expression analysis has been done by using the TaqMan gene expression array (Thermo-Fisher Scientific, Catalog #4331182) and Quant-Studio-5 device (Applied Biosystems). PCR reaction components were prepared using TaqMan™ Fast Universal PCR Master Mix (2X) kit (Applied Biosystems™ Cat. 4352042). Following TaqMan probes were used for qPCR analysis: *Gapdh* (Mm99999915_g1), *Vcan* (Mm01283063_m1), *Chst3* (Mm00489736_m1), *Chst7* (Mm00491466_m1), *Chst11* (Mm00517562_m1), *Chst12* (Mm00546416_s1).

Stereotaxic injection

For stereotaxic injection, two-month-old C57BL/6 male mice were sedated with isoflurane and secured to a stereotactic frame (SR-6M, Narishige Scientific Instrument Lab, Japan). The mice were anesthetized with isoflurane adjusted to 1.5-2% with oxygen levels at 0.4 L/min (Baxter 250ml Ch.-B.: 17L13A31). The body temperature was maintained at 37°C using a heating pad (ATC1000 from World Precision Instrument, USA) during the surgery. A calibrated glass microelectrode attached to an Ultra microinfusion pump (UMP3, World Precision Instrument, USA) was used to inject a volume of 1000 nL of the virus at a rate of 3 nL/sec using a 10 μL NanoFil syringe (World Precision Instrument, USA). A single injection per hemisphere was performed, using the following coordinates from the Bregma: AP: −1.9 mm, ML: ±1.5 mm, DV: −1.3 mm. Following the procedure, the animals were placed in a recovery chamber with red light for 15 minutes. Animals were used for experimental work 90 days after injection to allow successful knock-down of ECM molecules.

Electrophysiology

Preparation of acute hippocampal slices

Animals were anesthetized with isoflurane and decapitated. The brain was removed and cut into two hemispheres. Transverse slices with a thickness of 350 μm were obtained using a Vibroslicer (Leica, Nussloch, Germany) in an ice-cold cutting solution containing (in mM): 240 sucrose, 2 KCl, 2 MgSO4, 1.25 NaH2PO4, 25 NaHCO3, 1 CaCl2, 1 MgCl2, and 10 D-glucose (pH 7.3, adjusted with NaOH). The slices were kept in a carbogen-bubbled artificial cerebrospinal fluid (ACSF) containing (in mM): 120 NaCl, 2.5 KCl, 1.5 MgCl2, 1.25 NaH2PO4, 24 NaHCO3, 2 CaCl2 and 25 D-Glucose at RT for at least 60 minutes before recording. The slices were then transferred to a recording submerged chamber and perfused with ACSF at RT for fEPSP recordings. All solutions were saturated with 95% O2 and 5% CO2, and osmolality was maintained at 300 ± 5 mOsm.

fEPSPs recording in CA3-CA1 pathway

Glass electrodes filled with ACSF were used for stimulation and recording of fEPSPs. Monopolar stimulating glass electrodes were used to deliver 0.2 ms stimulation current pulses, and the stimulus-response curve was generated by applying increasing current pulses and monitoring the slope of evoked responses. For recordings of paired-pulse facilitation (PPF) and long-term potentiation (LTP), the stimulation intensity was selected based on the stimulus-response curve to elicit fEPSPs with a slope of 30% and 50% of the supramaximal fEPSPs, respectively. PPF was measured as the ratio of the slopes of the fEPSPs elicited by the second and first pulses given with 50 ms intervals. For LTP induction, theta-burst stimulation (TBS) protocol has been used, which included 5 trains of stimuli delivered at 20-sec intervals. Each train was composed of 10 stimulus bursts delivered at 5 Hz (200 ms interval) with each burst consisting of four pulses given at 100 Hz. The LTP value was calculated by comparing the mean slope of fEPSPs obtained 50-60 minutes after TBS to the mean slope of fEPSPs recorded 10 minutes before TBS. All recordings were obtained at RT using an EPC-10 amplifier (HEKA Elektronik, Germany). The recordings were digitized at 10-20 kHz and lowpass filtered at 1 kHz.

CS56-immunoprecipitation and mass spectrometry analysis in human postmortem tissue

Tissue preparation

Human postmortem amygdala sections were scraped from glass slides and homogenized by pipetting in homogenization buffer (320 mM sucrose, 5 mM Tris, pH 7.0) containing 1X HALT protease inhibitor cocktail (Thermo Fisher Scientific, Carlsbad, CA) and 1mg/ml heparin. Sample protein concentration was determined by a BCA protein assay (Thermo Fisher Scientific, Waltham, MA). For affinity purification, samples (3μg/μl) were aliquoted in 1 ml volumes with 1% TritonX-100 and 0.5% SDS and incubated overnight at 4°C. Samples for immunoblotting were boiled for 10 mins at 70°C in sample buffer (6X solution: 4.5% SDS, 15% β-mercaptoethanol, 0.018% bromophenol blue and 36% glycerol in 170 mM Tris-HCl, pH 6.8).

Immunoblotting

Twenty micrograms of protein were loaded onto 4-12% Novex NuPage Bis-Tris 10-well gels (1.5mm) (Life Technologies, Waltham, MA). Gels were run at 180 V for 1 hour and then transferred to PVDF membranes by Bio-Rad semidry transblotters (Bio-Rad, Hercules, CA, USA). All membranes were blocked by LiCor blocking buffer (LiCor, Lincoln, NE, USA) for 1 hour at room temperature. Membranes were probed overnight at 4°C for all primary antibodies. The antibodies used were: 1:500 mouse monoclonal CS56 (ab11570, Abcam, Cambridge, MA), 1:200 rabbit polyclonal Versican (sc-25831, Santa Cruz Biotechnology, CA, USA), 1:200 rabbit polyclonal (ab36861, Abcam, Cambridge, MA, USA). Following 3 x 10-minute washes in 1X PBS, membranes were incubated with appropriate IR-Dye 670 or 800cw labeled secondary antibodies (1:10,000) in LiCor blocking buffer for 1 hour at room temperature. Following 3 x 10-minute PBS washes, membranes were scanned using a LiCor Odyssey scanner.

CS56 affinity purification

CS56 affinity purification (AP) was performed by immunoprecipitation, using the Novex Life Technologies Dynabeads kit according to the manufacturer's guidelines, with some modifications. Briefly, 5 μg of antibody were conjugated per 1 mg of M-270 Epoxy beads (Life Technologies, Oslo, Norway) overnight at 37°C on a shaker. Beads were conjugated with CS56 (ab11570, Abcam Cambridge, MA, USA) or the corresponding isotype control IgM (sc-3881, Santa Cruz Biotechnology, Santa Cruz, CA, USA). The beads were rinsed 4 x 10 minutes in 1X PBS-T. Ten milligrams of antibody-conjugated beads were incubated overnight at 4°C with 742 μg of tissue homogenate. The following day, the supernatant was collected and retained for immunoblotting. Beads were rinsed (4 x 10-minute washes in 1X PBS-T) and the bound proteins were eluted in 30 μl of elution buffer (1 N ammonium hydroxide, 0.5 M EDTA, pH 11.6).

Mass spectrometry

CS56 affinity purified elutions were boiled at 70°C for 10 minutes in a sample buffer. The sample was loaded on a 1.5 mm, 4-12% gradient gels and electrophoresed until the sample ran 1.5 cm into the gel. Molecular weight markers (Thermo Spectra 26623) were run between the samples to indicate the protein-containing region of the gel. The gel was fixed in 50% ethanol/10% acetic acid overnight at RT, then washed in 30% ethanol for 10 min followed by two 10 min washes in MilliQ water (MilliQ Gradient system) and finally scanned on an Epson V700 scanner to record an image of the gel. The lanes were cut out of the gel, cut into small (~2mm) squares and were subjected to in-gel tryptic digestion and subsequent recovery of peptides.

Nano liquid chromatography coupled to electrospray tandem mass spectrometry (nLC-ESI-MS/MS) analyses were performed on a 5600+ QTOF mass spectrometer (Sciex, Toronto, On, Canada) interfaced to an Eksigent (Dublin, CA) nanoLC ultra nanoflow system. Samples were analyzed in technical duplicate. Protein was loaded (via an Eksigent nanoLC.as-2 autosampler) onto an IntegraFrit Trap Column (outer diameter of 360 μm, inner diameter of 100, and 25 μm packed bed) from New Objective, Inc. (Woburn, MA) at 2 μl/min in formic acid/H_2O 0.1/99.9 (v/v) for 15 min to desalt and concentrate the samples. For the chromatographic separation of peptides, the trap-column was switched to align with the analytical column, Acclaim PepMap100 (inner diameter of 75 μm, length of 15 cm, C18 particle sizes of 3 μm and pore sizes of 100 Å) from Dionex-Thermo Fisher Scientific (Sunnyvale, CA). The peptides were eluted using a variable mobile phase (MP) gradient from 95% phase A (Formic acid/H2O 0.1/99.9, v/v) to 40% phase B (Formic Acid/Acetonitrile 0.1/99.9, v/v) for 35 min, from 40% phase B to 85% phase B for 5 min and then keeping the same mobile phase composition for 5 additional min at 300 nL/min. The nLC effluent was ionized and sprayed into the mass spectrometer using NANOSpray® III Source (Sciex). Ion source gas 1 (GS1), ion source gas 2 (GS2) and curtain gas (CUR) were respectively kept at 12, 0 and 35 vendor-specified arbitrary units. The mass spectrometer method was operated in positive ion mode and the interface heater temperature and ion spray voltage were kept at 125°C, and at 2.6 kV respectively. Independent data acquisition (IDA) settings: For ions greater than:350 Da; from charge state:2 to 4; with intensity greater than:150; Switch after:30 spectra; Exclude for:30 sec; Mass tolerance:100 ppm; Ignore peaks within:6 Da; Fragment intensity multiplier:2; Maximum accumulation:2 sec; Maximum mass:1250 Da. The data was recorded using Analyst-TF (version 1.7) software.

QUANTIFICATION AND STATISTICAL ANALYSIS

All studies except proteomics

Data collection for all studies were carried out by investigators blind to experimental conditions. All statistics analyses were carried out using Prism8 software (GraphPad Software San Diego, CA). A Kolmogorov-Smirnov test was used to verify for normal distribution of the data before subjecting it to the appropriate test. The data in the text is all mean values ±SEM. Student's t-test for pairwise comparisons when the samples qualified for the normality test; otherwise, the Mann-Whitney test was used. The p-values represent the degree of significance as shown in the figures by asterisks (*$p < 0.05$, **$p < 0.01$, and ***$p < 0.001$). CBI was compared with the

predicted average =0.5 (reflecting a lack of inter-hemispheric differences) using a z-test. Mander's coefficients were calculated using the 'Colocalization Threshold' plug-in from ImageJ-FIJI software[57]. This software applies an unbiased auto-threshold strategy to prevent false-positive results (https://imagej.net/imaging/colocalization-analysis).

Details of statistical analyses, including the sample size (n indicates number of mice unless otherwise specified), statistical tests used, mean and standard error, p-values and 95% confidence intervals (C.I.) are included in the figure legends and in Tables S1–S5

Mouse proteomics

The raw LC-MS/MS data were searched using PeaksDB and PeaksPTM using Peaks Studio version Xpro (Bioinformatics Solutions, Inc., Waterloo, ON, Canada) against the Uniprot/Swissprot database for Mus musculus (house mouse) with a 1% false discovery rate and at least two unique peptides. A 10-ppm error tolerance for the precursor (MS1) and 0.02 Da mass error tolerance for fragment ions (MS2) were specified. A maximum of 3 missed cleavages per peptide was allowed for the database search, permitting non-tryptic cleavage at one end. Trypsin was specified as the enzyme, and carbamidomethylation as a fixed modification. A peaksPTM search was queued after the peaksDB search, using advanced settings of a larger set of variable modifications, including hydroxylation P, oxidation M, hydroxylation K, hydroxylation-Hex K, hydroxylation-Hex-Hex K, HexNAc ST, HexHexNAc ST, phosphorylation STY, ubiquitination K, deamidation N, methoxy K, and nitrotyrosine Y. The final protein list generated was a combination of peaksDB and peaksPTM searches. The label-free quantification was achieved using PEAKS Studio Quantification- a label-free module with a setting of mass error tolerance of 10 ppm and a retention time shift tolerance of 2.0 min. The normalization of the abundance for the label-free quantified proteins was performed using total ion chromatograms (TICs), and log transformation was performed using RStudio[67]. The identified proteins, peptides, and protein peptides list are provided as Supplementary Files 27. The label-free quantified proteins and log-transformed abundance protein lists are provided as Supplementary Files 8-11. The gene ontology (GO) annotation was performed using the DAVID Bioinformatics resource (https://david.ncifcrf.gov/). All the raw data is being available in the ProteomeXchange Consortium via the PRIDE[58] partner with the dataset ideintifier PXD047129 and https://doi.org/10.6019/PXD047129.

Human postmortem proteomics

All raw mass spectrometric files were searched against the human proteome (Uniprot, downloaded on September 29th 2022) including contaminants by MaxQuant (2.1.4.0)[68]. Label-free quantification with default settings was used. Briefly, Trypsin/P was set as digestion protease with up to two missed cleavages allowed, carbamidomethyl (cysteine) was included as a fixed modification and oxidation (methionine) and protein N-terminal acetylation were set as variable modifications. The FDR of protein and peptide identifications were filtered at 0.01. The iBAQ (Intensity Based Absolute Quantification) and match between runs options were enabled. Further downstream analysis of the data was performed with iBAQ values using Perseus v2.0.7.0.[69] Only protein groups detected in n=2 technical replicates in the CS56_IP were considered for further analysis. A subset of protein groups was identified in n=2 technical replicates in the CTL_IP. The correlation of sample replicates is presented in Figure S7.

Cell Reports, Volume *43*

Supplemental information

Focal clusters of peri-synaptic matrix contribute to activity-dependent plasticity and memory in mice

Gabriele Chelini, Hadi Mirzapourdelavar, Peter Durning, David Baidoe-Ansah, Manveen K. Sethi, Sinead M. O'Donovan, Torsten Klengel, Luigi Balasco, Cristina Berciu, Anne Boyer-Boiteau, Robert McCullumsmith, Kerry J. Ressler, Joseph Zaia, Yuri Bozzi, Alexander Dityatev, and Sabina Berretta

SUPPLEMENTAL MATERIAL

SUPPLEMENTAL SUPPORTING DATA

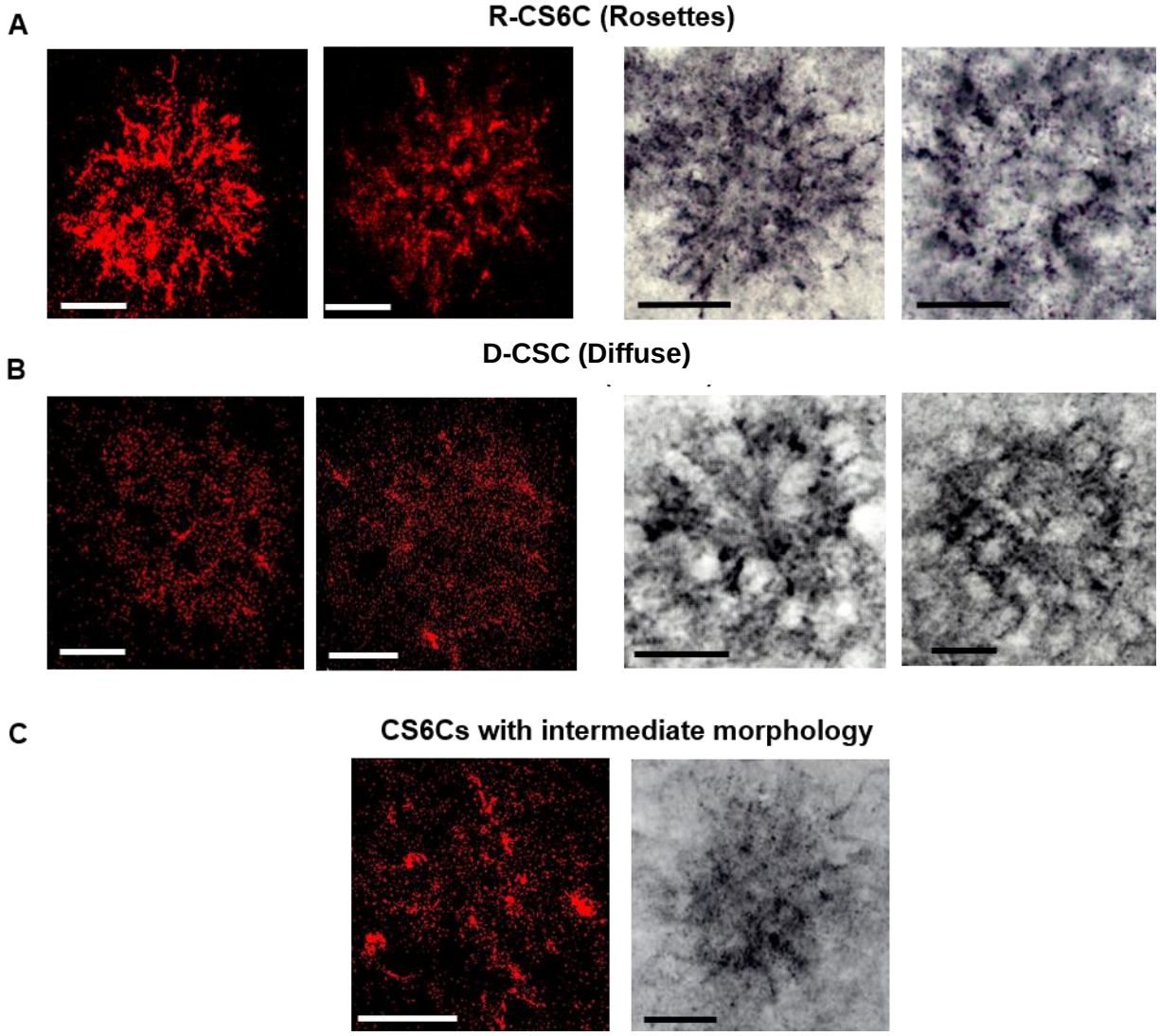

Fig. S1 Examples of CSCs in the mouse Barrel Cortex (related to Figure 1)

CSCs in the mouse BCx, immunolabeled with CS56 antibody and visualized with fluorescent (left) or light microscopy (right). The diameter of CSCs in mice is typically 50-75 μm. CSCs appear along a spectrum of morphological configurations. **A-B)** CSCs were classified in two main types, R-CSCs **(A)** and D-CSCs **(B)**. R-CSCs appear as predominantly composed of a multitude of intensely immunostained convergent processes. D-CSCs are predominantly of composed immunolabeled puncta. **C)** CSCs with intermediate morphology present with few labeled processes intermingled with dense puncta labeling. Scalebar (S.b.= 25μm).

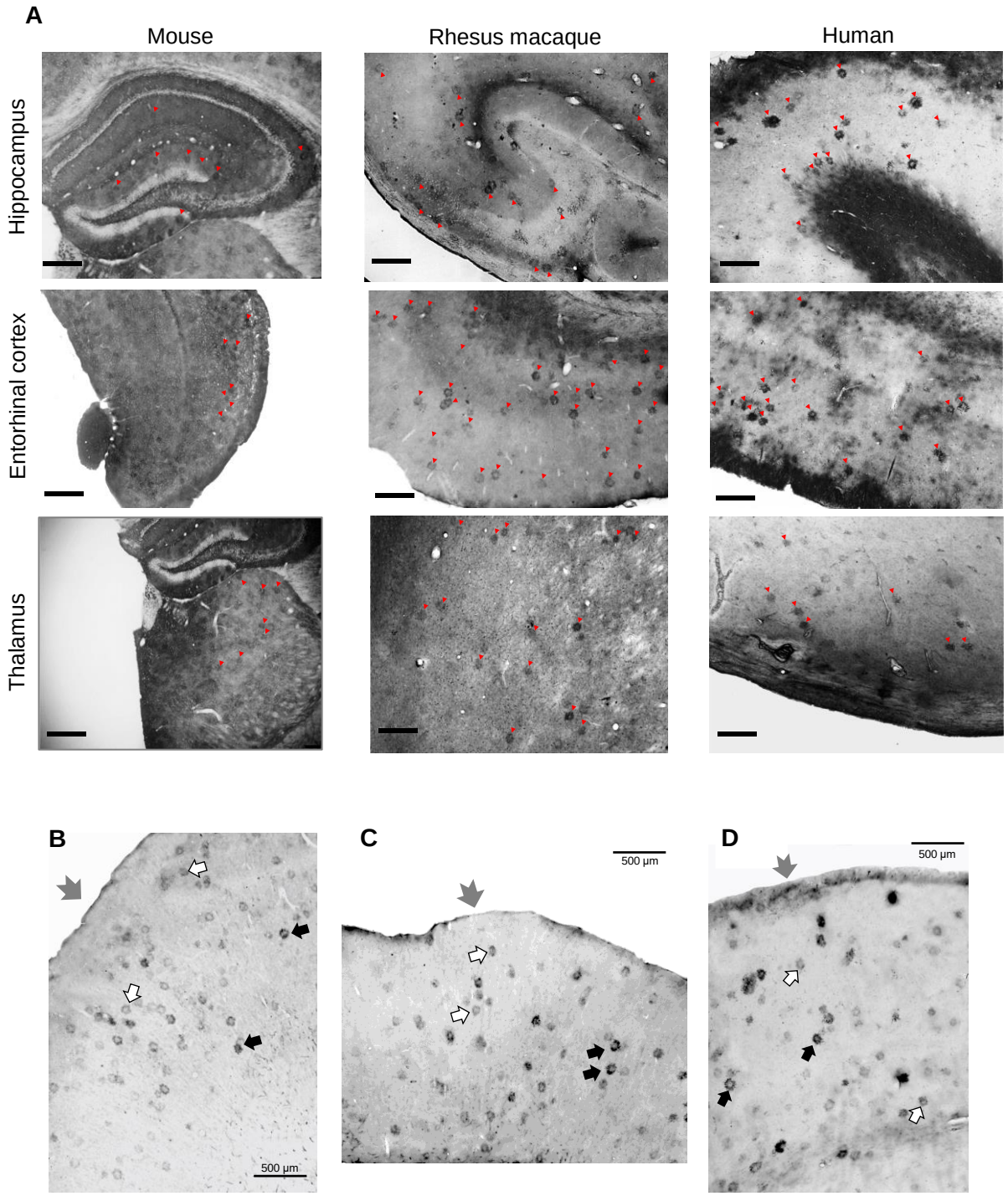

Fig. S2. CSCs populate cortical and subcortical regions in the mammalian brain.

(Related to figure 1). A) In line with previous literature, we observed that CSC are widespread in the postmortem brain of mouse, non-human primate, and human, showing remarkably conserved morphological appearance. In the mouse **(B)** non-human primate **(C)** and human **(D)** neocortex CSCs present in both R-CSC and D-CSC configurations (Black arrows: R-CSC. White arrows: D-CSC). Grey arrow indicates pial surface. S.b.= 500 µm.

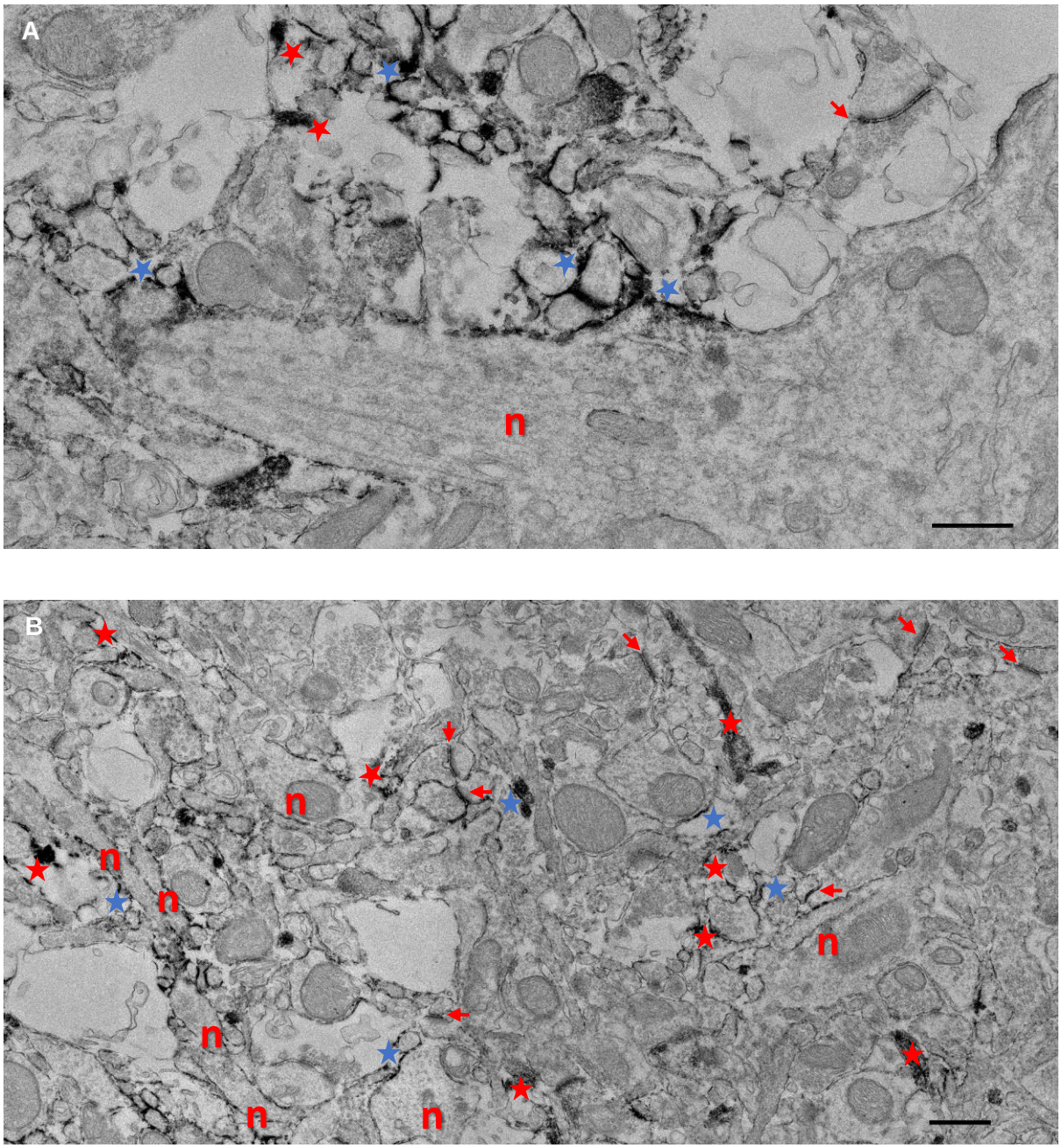

Fig. S3 CSC ultrastructural morphology in the mouse barrel cortex (BCx). (Related to figure 1) Electron microscopy studies in BCx investigated the ultrastructural characteristics of CSCs. Immuno-electron micrographs within a R-CSC **(A)** and a D-CSC **(B)** showing prominent immunoperoxidase reaction product within glial processes (red stars) and end-feet (blue stars), as well as within the synaptic cleft and around synaptic elements (red arrows). Note that some immunolabeling can also be detected on the outer surface of a dendritic plasma membrane, while the dendrite cytoplasm is void of labeling (S.b.= 500 nm). No CS56 immunolabeling is found within neuronal cells (intracellular neuronal elements, highlighted with red “n”).

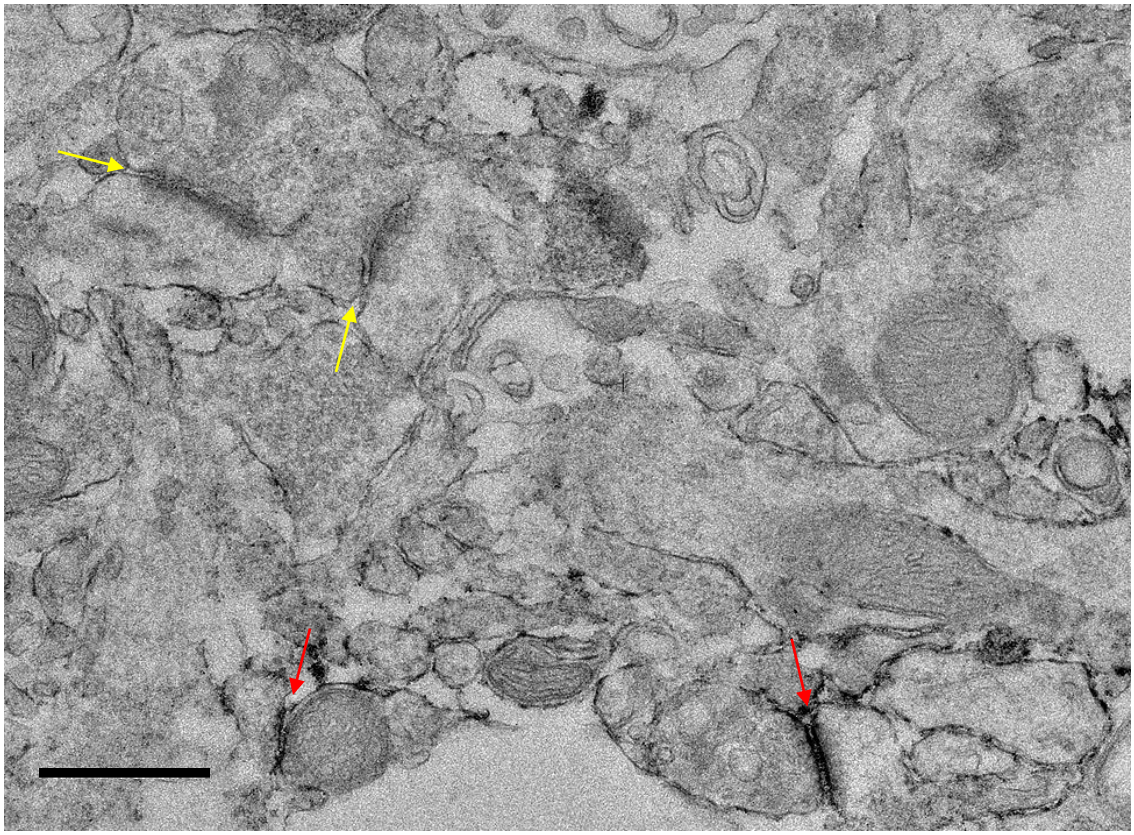

Fig. S4 Control for CSC ultrastructural morphology in the mouse barrel cortex (BCx).
(Related to figure 1).

As a control for the accuracy of the identification of CS56-IR synapses, we tested whether CS56 immuno-negative synapses could also be detected with CSCs. Immuno-electron micrograph within a “R-CSC” showing CS56-immunolabeled synapses (red arrows) in close proximity of immuno-negative synapses (yellow arrows) (S.b.= 500 nm).

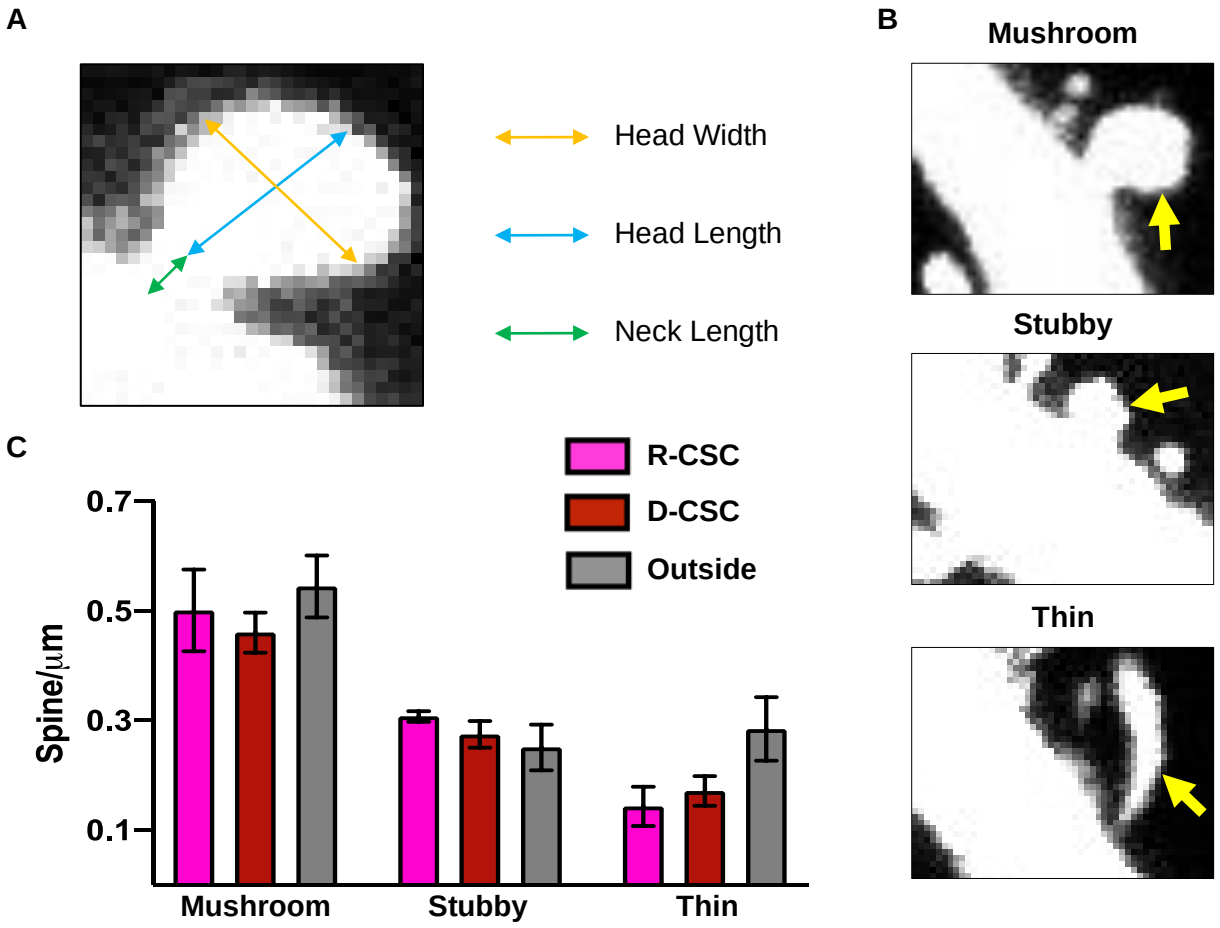

Fig. S5 Dendritic spines' analyses. (Related to figure 2).

As a first step toward testing the hypothesis that CSCs are associated with structural plastic changes at synapses, we assessed the dendritic spines' density within and outside CSCs. **A)** Representative picture showing the method for dendritic spine's measurement. Total spine length was obtained combining neck and head length. **B)** Confocal photomicrographs showing examples of mushroom, stubby and thin dendritic spines classification (yellow arrow). Classification of dendritic spines was performed according to the following criteria. *Mushroom* spines had clearly distinguishable spine head and neck, with the neck diameter significantly narrower than the head diameter. *Stubby* spines did not have a clearly distinct neck. *Thin* spines had a long, thin necks and heads and the total length of the spine was considerably greater than spine width. **C)** Dendritic spine density does not change within CSCs compared to outside; 2-way ANOVA, with Tuckey multiple comparisons: Mushrooms R-CSCs vs Outside p=0.869, C.I.= -0.2621 to 0.1745; D-CSCs vs Outside p=0.601, C.I.= -0.3026 to 0.134; R-CSCs vs D-CSCs p=0.913, C.I.=- -0.2115 to 0.2926. Stubby: R-CSCs vs Outside p=0.565, C.I.= -0.08135 to 0.1942; D-CSCs vs Outside p= 0.903, C.I.= -0.1142 to 0.1613; R-CSCs vs D-CSCs p=0.862, C.I.= -0.1262 to 0.1920. Thin: R-CSCs vs Outside p= 0.188, C.I.= -0.3368 to 0.05456; D-CSCs vs Outside p= 0.33, C.I.= -0.3089 to 0.08253; R-CSCs vs D-CSCs p= 0.947, C.I.= -0.2539 to 0.1980.

Error bar indicates SEM. * $p<0.05$.

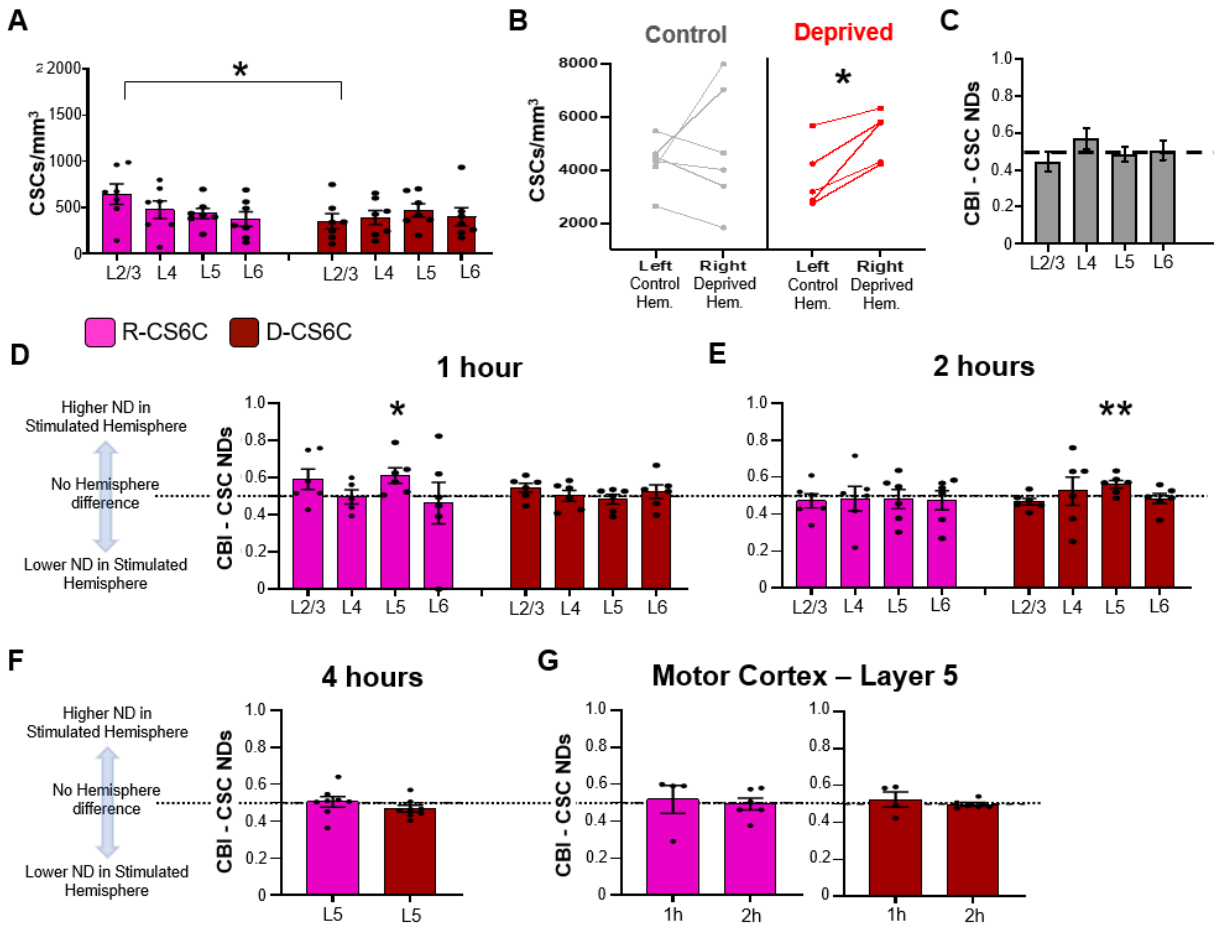

Fig.S6 Sensory manipulation. (Related to figure 3).

A) Estimated numerical densities show an increased prevalence of R-CSCs compared to D-CSCs in layer 2/3 (1-way repeated measure ANOVA: L2/3 p=0.031, C.I.= 30.09 to 557.6. L4 p=0.947, C.I.= -351,8 to 521,0. L5 p=0.991, C.I.= -327.4 to 259.6. L6 p=0.999, C.I.= -510.5 to 462.2). **B)** CSC numerical densities (NDs) in the BCx do not differ between hemispheres in control animals; paired t-test: p=0.55, C.I.= -1649 to 2721), but are significantly decreased in the deprived hemisphere of sensory-deprived animals with respect to the control hemisphere; paired t-test, p=0.01, C.I.= 479.6 to 2521. **C)** Contralateral bias index (CBI) analysis in control mice shows comparable CSCs-NDs between hemispheres across layers. (z test CBI: L2/3 p=0.29, C.I.= -0.1992 to 0.08437. L4 p=0.22, C.I.= -0.07495 to 0.2105. L5 p=0.68, C.I.= -0.1174 to 0.08567. L6 p=0.92, C.I.= -0.1322 to 0.1433)**. D)** Whisker stimulation drives layer 5 selective increase in R-CSCs 1 h post-stimulation (z test L2/3 p=0.094, C.I.= -0.04980 to 0.2336. L4 p=0.904, C.I.= -0.1096 to 0.1025. L5 p=0.017, C.I.= 0.003703 to 0.2200. L6 p=0.603, C.I.= -0.3241 to 0.2516), but has no effect on D-CSCs in layer 5 and 6 (z test L2/3 p=0.114, C.I.= -0.01707 to 0.1078. L4 p=0.535, C.I.= -0.07298 to 0.07847. L5 p=0.496, C.I.=-0.08268 to 0.05084. L6 p=0.589, C.I.= -0.07063 to 0.1202). **E)** Whisker stimulation drives layer 5 selective increase in D-CSC 2 h post-stimulation (z test L2/3 p=0.067, C.I.= -0.1256 to 0.06996. L4 p=0.741, C.I.= -0.1872 to 0.1542. L5 p=0.003, C.I.= -0.1503 to 0.1148. L6 p=0.568, C.I.= -0.1579 to 0.1076), but has no effect on R-CSCs in layer 5 and 6: z test L2/3 p=0.465, C.I.= -0.07760

to 0.01314. L4 p=0.802, C.I.= -0.1716 to 0.2216. L5 p=0.727, C.I.= 0.006922 to 0.1168. L6 p=0.624, C.I.= -0.08330 to 0.05320. **F)** No changes in R-CSCs or D-CSCs were detected 4 h post whisker stimulation; z-test R-CSCs p=0.859, C.I.= -0.06015 to 0.07032; D-CS6Cs p=0.1196, C.I.= -0.07390 to 0.01058.**G)** A control brain region, i.e. layer 5 of the motor cortex, do not show significant differences at neither 1- or 2-hour time points after whisker stimulation; z-test 1hr: R-CSCs p=0.97, C.I.= -0.2230 to 0.2600, D-CSCs p=0.57, C.I.= -0.1060 to 0.1532. 2hr: R-CSCs p=0.77, C.I.= -0.08783 to 0.07398, D-CSCs p=0.68, C.I.= -0.02647 to 0.02251.

Error bar indicates SEM. * p<0.01 / ** p<0.001

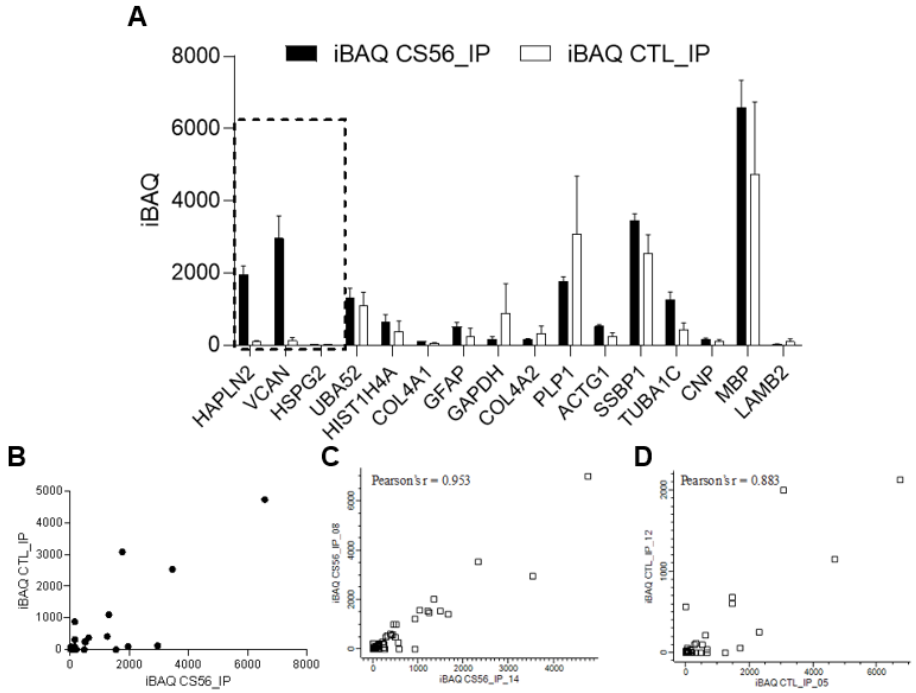

Fig.S7 Versican association with CS56-reactive CSPGs is confirmed in human postmortem brain. (Related to Figure 4).

A) Comparison between CS56-IP and CTL-IP confirms the enrichment of Versican in the postmortem human amygdala. **B)** Correlation of CTL_IP and CS56_IP protein iBAQ values. **C)** and **D)** Correlation of protein iBAQ values for (**C**) CS56_IP technical replicates and (**D**) CTL_IP technical replicates. iBAQ= intensity based absolute quantification; CTL= control.

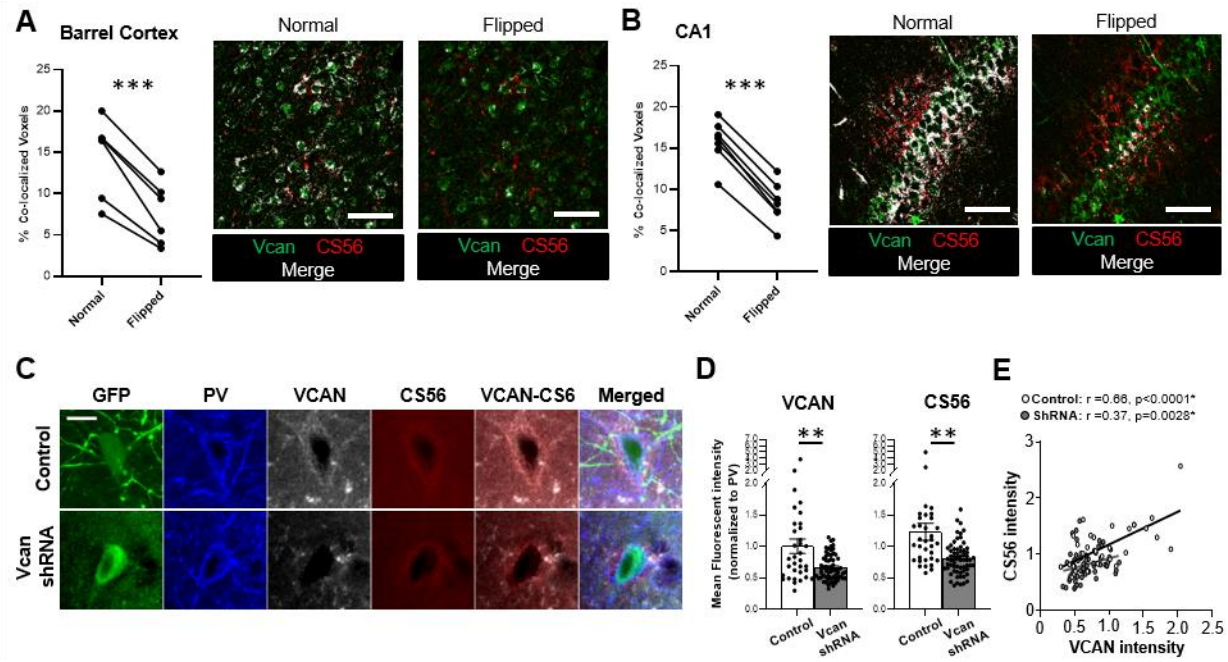

Fig. S8. CS56-reactive glycans and versican are functionally related. (Related to figure 5).

A) and **B)** Negative control comparison for Vcan-CS56 co-localization analysis. Artificially flipping one of the two colors channels (Red-CS56) along the horizontal plane the percentage of colocalized pixels significantly decrease compared to what observed in the original photomicrographs, confirming the specificity of CS56 and Vcan co-localization; paired t-test Barrel Cortex: p=0.0007, C.I.= -9.338 to -4.535. CA1: p<0.0001, C.I.= -8.173 to -6.670. **Left panels**; graph showing the difference in co-localized pixels before and after flipping the red channel horizontally. **Center panels**; pixel maps visually depicting the colocalization between Vcan and CS56 (in white) identified on the original images**. Right panels**; pixel maps visually depicting the colocalization between Vcan and CS56 (in white) after the red channel was artificially flipped horizontally. S.b.=50 µm**. C)** Representative photomicrograph showing CS56-Vcan co-localization around a parvalbumin-positive (PV) neuron in a control hippocampus (top) and their reduced intensity in a mouse treated with Vcan-ShRNA (bottom). GFP signal identifies the injected AAV carrying control and Vcan-ShRNA. S.b.= 20 µm. **D)** Total amounts of Vcan and CS56 are similarly reduced by Vcan-ShRNA treatment in the mouse hippocampus. n=34 Controls, n=53 Vcan-ShRNA*;* t-test: Vcan p=0.004, C.I.= -0.5198 to -0.1552; CS56 p=0.001, C.I.= -0.6372 to -0.2132. **E)** Vcan and CS56 intensity is positively correlated in the control condition and after Vcan-ShRNA expression. Vcan-CS56 correlation; Control: Pearson r=0.64, p<0.0001, C.I.= 0.4168 to 0.8209. Vcan-ShRNA: Sperman r=0.37, p=0.0028, C.I.= 0.1280 to 0.5715. Error bar indicates SEM. ** p<0.001. *** p<0.0001.

	Percentage of PSD95-IR elements juxtaposed to CS56-IR puncta	
	Mean	SEM
Outside CSC	3.22%	0.59
Inside CSC	5.91%	0.82

Table S1. Comparison of PSD95-IR elements juxtaposed to CS56-IR puncta within D-CSCs as compared outside CSC. (Related to figure 1).

Percentages of PSD95-IR puncta juxtaposed to CS56-IR puncta are significantly higher within CSCs as compared to an equivalent area adjacent to them ($p=0.004$). Measurements were carried on Z-stacks of images obtained by confocal microscopy on the BCx of naïve wild type mice ($n=3$). Five CSCs and 5 adjacent areas of the same size were counted for this analysis.

Spine Type	Cluster Type	Mean	SEM	p value (1-way ANOVA)
Mushroom Spines	D-CSC	0.48	0.04	0.618
	R-CSC	0.50	0.07	
	Outside CSC	0.54	0.05	
Stubby Spines	D-CSC	0.29	0.03	0.592
	R-CSC	0.3	0.009	
	Outside CSC	0.25	0.04	
Thin Spines	D-CSC	0.17	0.02	0.152
	R-CSC	0.14	0.03	
	Outside CSC	0.28	0.05	

Table S2. (related to figure 2) Densities of dendritic spines morphologically identified as 'mushroom', 'stubby' and 'thin' (see Fig. S5) are not significantly different on dendrites embedded within D- or R- CSCs (n=5/CSC type) and dendrites not associated with CSCs (n=5). Measurements were taken in n=5 mice.

CSC type	Spine measure	Location *(within/outside CSC)*	Mean ± SEM (μm)	Mann-Whitney test
R-CSC	Head Width	Within	0.56 ± 0.01	**<0.001**
		Outside	0.45 ± 0.01	
	Head length	Within	0.56 ± 0.01	**0.004**
		Outside	0.61 ± 0.01	
	Neck length	Within	0.44 ± 0.01	0.347
		Outside	0.45 ± 0.01	
D-CSC	Head Width	Within	0.57 ± 0.01	**0.024**
		Outside	0.61 ± 0.01	
	Head length	Within	0.63 ± 0.01	**0.047**
		Outside	0.66 ± 0.01	
	Neck length	Within	0.44 ± 0.01	**0.012**
		Outside	0.51 ± 0.01	

Table S3. Dendritic spine geometry changes within R- and D- CSCs. (Related to figure 2)

Within R-CSCs, mushroom spines have wider and shorter head, but unaltered neck length (n=194 spines over 4 dendrites) with respect to dendritic spines located on dendrites in the immediate vicinity, but outside, R-CSCs (n=154 spines over 4 dendrites). Wider and shorter spine heads within R-CSC are interpreted to reflect synaptic potentiation. In contrast, within D-CSCs, mushroom spines have narrower and shorter head width and neck length (n=217 spines over 6 dendrites) with respect to dendritic spines located on dendrites outside D-CSCs (n=206 spines over 6 dendrites). The narrower head width potentially reflects synaptic de-potentiation.

Group	Hemisphere/layer	Mean	SEM	CBI	CBI SEM	n mice	Paired t-test	Z-test (CBI)
Control Mice	Right Hem.	4817.9	940.91	0.49	0.04	6	0.555	0.865
	Left Hem.	4281.81	378.37					
	L2/3 Right Hem.	1517.91	444.57	0.55	0.05	6	0.259	0.298
	L2/3 Left Hem.	1001.86	122.003					
	L4 Right Hem.	992.76	229.74	0.43	0.05	6	0.443	0.222
	L4 Left Hem.	1189.76	153.67					
	L5 Right Hem.	1223.18	168.76	0.51	0.03	6	0.405	0.689
	L5 Left Hem.	1081.78	83.98					
	L6 Right Hem.	1084.03	227.44	0.54	0.05	6	0.771	0.92
	L6 Left Hem.	1008.4	107.09					
Sensory Deprived Mice	Right Hem.	4827.9	519.43	0.4	0.02	5	**0.015**	**<0.001**
	Left Hem.	3412.66	547.69					
	L2/3 Right Hem.	1583.93	257.9	0.39	0.01	5	**0.016**	**<0.001**
	L2/3 Left Hem.	969.3	154.02					
	L4 Right Hem.	1109.42	65.58	0.41	0.06	5	0.332	0.126
	L4 Left Hem.	848.61	227.53					
	L5 Right Hem.	1519.48	202.71	0.45	0.02	5	0.071	**0.013**
	L5 Left Hem.	1162.97	98.99					
	L6 Right Hem.	944.5	287.62	0.46	0.09	5	0.468	0.631
	L6 Left Hem.	675.97	113.04					

Table S4. (Related to figure 3) Unilateral whisker trimming (1 week) significantly decreases CSCs-NDs in the contralateral BCx. This effect is predominantly driven by changes in layer (L) 2/3 and L5. No inter-hemispheric difference is observed in a group of untreated animals (controls).

CX area /layer	Survival time	Cluster type	Hemisphere	Mean	SEM	CBI	CBI SEM	Paired t-test	Z-test (CBI)
BCx L5	1 hr	R-CSC	Stimulated	241.16	47.53	0.61	0.03	0.051	**0.017**
			control	160.6	39.66				
		D-CSC	Stimulated	1181.26	85.98	0.48	0.02	0.584	0.496
			control	1268.20	160.94				
	2 hr	R-CSC	Stimulated	514.01	97.37	0.48	0.05	0.742	0.727
			control	545.06	85.43				
		D-CSC	Stimulated	1621.73	196.15	0.58	0.01	**0.03**	**0.003**
			control	1235.95	113.57				
BCx L6	1 hr	R-CSC	Stimulated	137.81	21.31	0.55	0.06	0.801	0.410
			control	121.9	28.01				
		D-CSC	Stimulated	891.24	126.58	0.53	0.04	0.537	0.580
			control	819.93	97.07				
	2 hr	R-CSC	Stimulated	466.63	92.65	0.47	0.05	0.951	0.624
			control	471.62	72.18				
		D-CSC	Stimulated	909.18	136.34	0.48	0.02	0.66	0.568
			control	942.28	132.3				
Motor CX L5	1 hr	R-CSC	Stimulated	367.24	62.4	0.51	0.07	0.970	0.833
			control	372.53	85.1				
		D-CSC	Stimulated	1064.82	73.75	0.52	0.04	0.574	0.582
			control	1061.29	97.47				
	2 hr	R-CSC	Stimulated	502.76	92.70	0.49	0.03	0.775	0.825
			control	487.05	89.6				
		D-CSC	Stimulated	912.71	136.35	0.49	0.009	0.687	0.833
			control	927.93	154.24				

Table S5. Numerical densities (NDs) of CSC increase in response to sensory stimulation.

(Related to figure 3)

In layer 5 of the BCx, NDs of R-CSC are increased at 1 hour survival time (i.e. sacrificed 1 hour following the end of passive whisker stimulation). D-CSC NDs are not altered at this time point. Conversely, at 2 hours survival time, NDs of R-CSCs are not altered, but NDs of D-CSC are significantly increased. To test for cortical area- and layer-specificity of this effect, R- and D- CSCs were counted in layer 5 of the motor cortex and layer 6 of the BCx. No changes were detected in either region/layer.

Accession	Description	Coverage	#Peptides	#Unique	Log transformed Normalized abundance
Q9JKS5|HABP4_MOUSE	Intracellular hyaluronan-binding protein 4	29	13	13	17,25567542
Q9R1V7|ADA23_MOUSE	Disintegrin and metalloproteinase domain-containing protein 23	12	8	8	16,93906235
Q61361|PGCB_MOUSE	Brevican core protein	9	6	6	16,47385217
Q9R1V4|ADA11_MOUSE	Disintegrin and metalloproteinase domain-containing protein 11	8	5	5	16,45751946
Q62059|CSPG2_MOUSE	Versican core protein	2	4	4	16,27121
Q61282|PGCA_MOUSE	Aggrecan core protein	1	2	2	15,11806651
P55066|NCAN_MOUSE	Neurocan core protein	3	3	3	14,0380527

Table S6. CS56 epitope-carrying ECM molecules and binding partners from the mouse primary somatosensory cortex. List of quantified CSPGs core-proteins and other ECM-relevant proteins identified after CS56-IP from S2, containing the light membrane fractions, after in-gel trypsin digestion and LC-MS/MS proteomic analysis. **(Related to figure 4)**

					Log IBAQ		
Accession	Description	Coverage	#Peptides	#Unique	Replicate #1	Replicate #2	Average
VCAN	Versican core protein	6.8	19	19	3,554464931	3,369939079	3,462202005
BCAN	Brevican core protein	9.5	8	7	2,298197867	2,37524283	2,336720349
NCAN	Neurocan core protein	10.9	14	13	3,260786669	3,110017007	3,185401838
HAPLN1	Hyaluronan and proteoglycan link protein 1	14.4	4	4	2,673693496	2,69651365	2,685103573
HAPLN2	Hyaluronan and proteoglycan link protein 2	32.9	12	12	3,341573002	3,237015629	3,289294315
GFAP	Glial fibrillary acidic protein	14.8	5	4	2,797475288	2,594127251	2,695801269

Table S7. CS56 epitope-carrying ECM molecules and binding partners from the postmortem human amygdala. **(Related to figure 4)**
List of quantified CSPGs core-proteins and other ECM relevant proteins identified after CS56-IP from a single specimen of human postmortem amygdala. **(Related to figure 4)**

Accession	Description	Coverage	#Peptides	#Unique	Log transformed Normalized abundance
P46096|SYT1_MOUSE	Synaptotagmin-1	58	52	34	20,61233712
Q64332|SYN2_MOUSE	Synapsin-2	58	56	46	19,70134066
O88935|SYN1_MOUSE	Synapsin-1	57	40	33	19,4485771
Q8BG39|SV2B_MOUSE	Synaptic vesicle glycoprotein 2B	21	18	18	18,36962087
Q8JZP2|SYN3_MOUSE	Synapsin-3	42	21	16	18,36331327
Q9R1V7|ADA23_MOUSE	Disintegrin and metalloproteinase domain-containing protein 23	13	9	9	17,0835636
P46097|SYT2_MOUSE	Synaptotagmin-2	43	25	8	16,79523322
Q62277|SYPH_MOUSE	Synaptophysin	11	4	4	16,07440527
Q9R0N7|SYT7_MOUSE	Synaptotagmin-7	14	5	5	15,76521262
Q9R1V6|ADA22_MOUSE	Disintegrin and metalloproteinase domain-containing protein 22	9	7	7	15,16368848
O55100|SNG1_MOUSE	Synaptogyrin-1	10	2	2	14,89585767
Q9R1V4|ADA11_MOUSE	Disintegrin and metalloproteinase domain-containing protein 11	6	4	4	14,58893584
Q8R191|SNG3_MOUSE	Synaptogyrin-3	15	3	3	14,46021302
Q9JIS5|SV2A_MOUSE	Synaptic vesicle glycoprotein 2A	5	3	3	14,16995719

Table S8. CS56 synaptic carriers/binding partners from the mouse BCx. List of quantified proteins implicated in synaptic plasticity identified after CS56-IP from P2, containing crude synaptosomal fractions, after in-gel trypsin digestion and LC-MS/MS proteomic analysis. **(Related to figure 4)**

	Subject	% Vcan overlapping with CS56	% CS56 overlapping with Vcan
BCX	Mouse 1	0.5251	0.5429
	Mouse 1	0.5195	0.5212
	Mouse 1	0.5799	0.5653
	Mouse 2	0.527	0.5027
	Mouse 3	0.3215	0.4312
	Mouse 3	0.2692	0.4024
HPC	Mouse 1	0.5587	0.5285
	Mouse 1	0.4744	0.482
	Mouse 1	0.3938	0.3856
	Mouse 2	0.5006	0.5222
	Mouse 2	0.4945	0.4797
	Mouse 3	0.515	0.5028
	Mouse 3	0.5464	0.5436

Table S9. Co-localization between versican and CS56. (Related to figure 5)

Mander's coefficients reflect the degree of co-localization between Versican and CS56 in both BCx and hippocampus